Top Quark Mass Measurement Using the Template Method in the Lepton + Jets Channel at CDF II

The CDF Collaboration

URL http://www-cdf.fnal.gov

(Dated: April 6, 2005)

Abstract

This report presents a measurement of the top quark mass using the CDF run II detector at Fermilab. Colliding beams of protons and anti-protons at Fermilab's Tevatron ($\sqrt{s} = 1.96$ TeV) produce top/anti-top pairs, which decay to $W^+W^-b\bar{b}$; events are selected where one W decays hadronically, and one W decays to either e or μ plus a neutrino. The data sample was collected between March 2002 and September 2003, and corresponds to an integrated luminosity of 318 pb^{-1}. One hundred and thirty-five candidate $t\bar{t}$ events are separated into four subsamples based on jet transverse energy thresholds and the number of b jets identified by a displaced vertex. In each event, the best fit top quark invariant mass is determined by minimizing a χ^2 for the overconstrained kinematic system. At the same time, the hadronically decaying W boson is reconstructed in the same event sample. The comparison of the precisely known and observed W boson mass provides an independent *in situ* determination of the energy scale of the hadronic jets. A simultaneous likelihood fit of the reconstructed top quark masses and the W boson invariant masses in the data sample to distributions from simulated signal and background events gives a top mass of $173.5\ ^{+3.7}_{-3.6}$ (stat.) ± 1.7 (syst.) GeV/c^2. This technique provides a 22% reduction in the uncertainty in the jet energy scale, the dominant systematic uncertainty in this measurement. This is the most precise single measurement of the top quark mass. A measurement made without the simultaneous constraint on the *in situ* jet energy scale calibration yields a consistent top quark mass value of $measAStatSyst173.22.92.83.4$ GeV/c^2..

PACS numbers: Valid PACS appear here

I. INTRODUCTION

A precision measurement of the top quark mass is one of the primary goals of the upgraded Tevatron accelerator and its two general-purpose detectors. In addition to being a fundamental parameter of the Standard Model, the large top quark mass may indicate a special role for the top quark in electroweak symmetry breaking. Due to the top quark's large contribution to radiative corrections, a more accurate measurement will make precision tests of the Standard Model more powerful, and provide tighter constraints on the mass of the putative Higgs particle.

This article reports a measurement of the top quark mass in the lepton + jets decay channel using the CDF detector at Fermilab, with 318 pb^{-1} of collision data collected in run II, between March 2002 and August 2004. A brief overview of the analysis is as follows. We scrutinize the data for events where a $t\bar{t}$ pair has been produced and has decayed to two W bosons and two b quarks, where subsequently one W boson decayed to two quarks, and the other W boson decayed to an electron or muon and a neutrino. Thus we look for a high-energy isolated electron or muon, missing energy representing the neutrino, two jets of particles corresponding to the b quarks, and two additional jets corresponding to the hadronic W decay.

We determine the mass of the top quark using a single quantity, the reconstructed top quark mass attempting a full-reconstruction of both top quark candidates in each event. This quantity is strongly dependent on the top quark pole mass. We compare the distribution of the reconstructed mass from events in the data with the distributions derived from events randomly generated and simulated at various values of the top mass. We also simulate events from the expected background processes. The top quark mass whose simulated events, when combined with the background, best describe the distribution in the data, is our measured value. We improve the power of the method by separating the events into four subsamples that have different background contamination and different sensitivity to the top mass.

For the quantity to be compared between data and simulated events, we choose the reconstructed top quark mass, determined in each event by minimizing a χ^2 expression for the resolutions and kinematic relationships in the $t\bar{t}$ system. The mass reconstruction is complicated by the fact that we don't know which jet represents each quark in the event. However, since we know something about the intermediate states of the $t\bar{t}$ system, such as

the W mass, the system is overconstrained, and we can choose which jet to assign to which quark based on the fit quality.

The dominant systematic uncertainty in this measurement arises from the determination of the jet energy scale for the top quark daughter jets, the two b-quarks in the event and the two jets from the W boson decay. We have developed a technique to use the fact that the W boson daughters should form a dijet invariant mass that is consistent with the precisely know W boson. We show that this jet energy scale information is largely independent of the top quark mass, and can be used to significantly reduce the uncertainties in the overall top quark mass measurement. We also make a measurement of the top quark mass without this additional information and obtain consistent results.

The method used is similar in spirit to an analysis performed at CDF using data from run I [**?**]. Combined with other analyses that use more sophisticated techniques [**?** **?**], this approach has several advantages. First, many parts of the detector, as well as all of the offline software, are new with respect to run I. By performing an analysis similar to the one previously published, we can draw on the experience and expertise developed in run I and gain confidence in our run II tools and methods. Second, this analysis is based on kinematic reconstruction of the top quark final state, and as such makes fewer assumptions than methods based on the full Standard Model matrix element for $t\bar{t}$ production and decay. Finally, this measurement can be combined with measurements using the other techniques, so that we can take full advantage of non-overlapping statistical and systematic uncertainties.

II. DETECTOR, BACKGROUNDS, AND EVENT SELECTION

This section begins with an explanation of the $t\bar{t}$ event signature along with a summary of the background processes that can mimic it. The relevant parts of the CDF detector are briefly described. The event selection and the separation into disjoint subsamples are defined next. Finally, the expected number of background events is discussed.

A. Event Signature

The Standard Model top quark decays into a W boson and a b quark, immediately ($\tau \approx 4 \times 10^{-25}$ s) and with $\sim 100\%$ branching ratio. The $t\bar{t}$ event signature is therefore

determined by the decay products of the two Ws, each of which can produce two quarks or a charged lepton and a neutrino. This analysis considers events in the lepton + jets channel, where one W decays to quarks and the other W decays to $e\nu_e$ or $\mu\nu_\mu$. In the following, a lepton candidate will refer exclusively to an electron or a muon candidate. Thus, interesting events have a high-p_T isolated e or μ, a neutrino, and four jets, two of which are b jets. More jets may be present due to hard gluon radiation from an incoming parton (initial state radiation or ISR) or from a final-state quark (final state radiation or FSR).

There are several non-$t\bar{t}$ processes that have similar signatures and enter into the event sample for this analysis. Events where a leptonically decaying W boson is found in association with QCD production of at least four additional jets, sometimes including a $b\bar{b}$ pair, have the same signature and are an irreducible background. Singly produced top quarks, e.g. $q\bar{q} \to t\bar{b}$, with a leptonic W decay and additional jets produced via QCD radiation, also have the same signature. Additional background events enter the sample when the $t\bar{t}$ signature is faked. For example, a jet can fake an isolated lepton with very low efficiency, a neutrino can be mistakenly inferred when the missing energy in the event is mismeasured, and a leptonically decaying Z boson can look like a W if one lepton goes undetected.

B. Detector

The Collider Detector at Fermilab is a general-purpose detector observing $p\bar{p}$ collisions at Fermilab's Tevatron. The detector geometry is cylindrical, with the z axis pointing along a tangent to the Tevatron ring, in the direction of proton flight in the accelerator. Transverse quantities such as E_T and p_T are projections into the plane perpendicular to the z axis. The coordinates x, y, r, and ϕ are defined in this transverse plane, with the x axis pointing outward from the accelerator ring, and the y axis pointing straight up. The angle θ is the polar angle measured from the proton direction, and $\eta = -\frac{1}{2}\ln(\tan\theta)$ is the pseudorapidity. When η is calculated assuming a reconstructed interaction point ($z \neq 0$), it is referred to as η_{evt}. Figure 1 shows an elevation view of the CDF detector. The relevant subdetectors are described briefly below. A more complete description of the CDF run II detector is provided elsewhere [**?**].

The CDF tracking system is the first thing seen by a particle leaving the interaction point. The silicon detectors [**?**] provide position measurements with very high resolution for

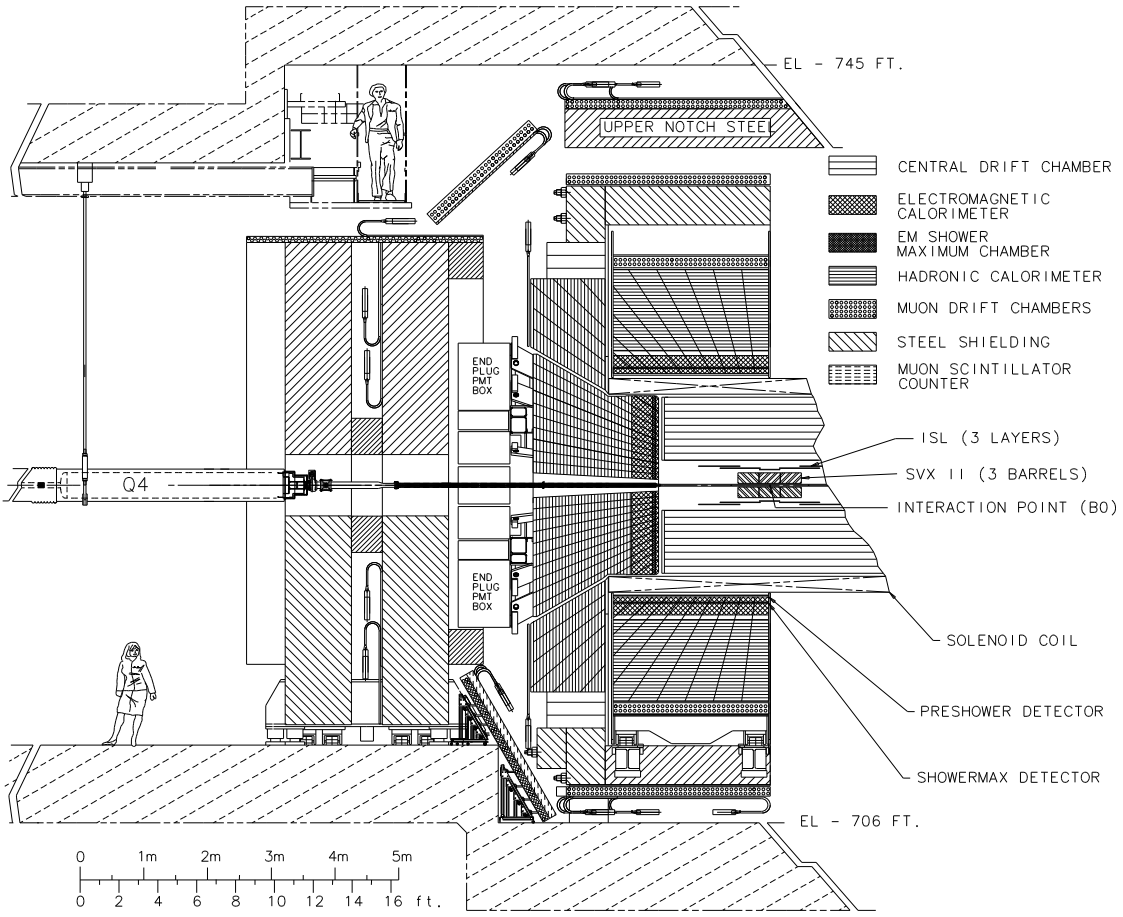

FIG. 1: An elevation view of the CDF run II detector. From inside to outside, CDF consists of a silicon strip detector, a tracking drift chamber, an electromagnetic calorimeter, a hadronic calorimeter, and muon chambers.

charged particles close to the interaction region, allowing extrapolation of tracks back to the collision point and reconstruction of secondary, displaced vertices. There are three separate silicon microstrip subdetectors, in which all but the innermost layer use double-sided wafers of silicon to get measurements in both axial and stereo directions for three-dimensional tracking. There are a total of 722,432 channels, with a typical strip pitch of 55–65 μm for axial strips, 60–75 μm for 1.2° small-angle stereo strips, and 125–145 μm for 90° stereo strips. The innermost detector, layer 00 (L00), is a single-sided layer of silicon mounted directly on the beampipe, at a radius of about 1.6 cm, providing an axial measurement as close to the collision point as possible. The SVXII detector is 90 cm long and contains 12 wedges in ϕ, each with 5 layers of silicon at radii from 2.5 cm to 10.6 cm. One side of each layer contains strips oriented in the axial direction, and the other side contains 90° stereo strips in

three cases, and 1.2° small-angle stereo strips in two cases. The Intermediate Silicon Layers (ISL) comprise three layers of silicon at larger radii: one at 22 cm for $|\eta| < 1$, and two at 20 cm and 28 cm for $1 < |\eta| < 2$. Besides providing extra measurements between the drift chamber and SVXII to ease track reconstruction in the central region, the ISL also allows tracks to be reconstructed at high η with larger level arm, and therefore better momentum resolution, since drift chamber coverage drops off in the region $1 < |\eta| < 2$.

The Central Outer Tracker (COT) [**?**] measures particle locations over a large radial distance, providing precise measurements of track curvature. It is a large open-cell drift chamber with 8 "superlayers" (4 axial and 4 with a 3° stereo angle), each of which contains 12 wire layers, for a total of 96 layers. There are 30,240 wires in total. The COT occupies a volume 310 cm in length and between radii of 43 cm and 130 cm. A magnetic field of 1.4 T is provided by a superconducting solenoid surrounding the silicon detectors and central drift chamber.

Particle energies are measured using sampling calorimeters. The calorimeters are segmented into towers with projective geometry. The segmentation of the CDF calorimeters is rather large, so that often several particles contribute to the energy measured in one tower.

In the central region, i.e. $|\eta| < 1.1$, the calorimeter is divided into wedges subtending 15° in ϕ. Each wedge has ten towers, of roughly equal size in η, on each side of $\eta = 0$. The central electromagnetic calorimeter (CEM) [**?**] contains alternating layers of lead and scintillator, making 18 radiation lengths of material. The transverse energy resolution for high-energy electrons and photons is $\frac{\sigma(E_T)}{E_T} = \frac{13.5\%}{\sqrt{E_T}} \oplus 1.5\%$. Embedded in the CEM is a shower maximum detector, the CES, which provides good position measurements of electromagnetic showers and is used in electron identification. The CES consists of wire proportional chambers with wires and cathode strips providing stereo position information. The central hadronic calorimeter (CHA) and the end wall hadronic calorimeter (WHA) [**?**] are of similar construction, with alternating layers of steel and scintillator (4.7 interaction lengths). The WHA fills a gap in the projective geometry between the CHA and the plug calorimeter.

The calorimetry in the end plugs ($|\eta| > 1$) is new for run II. In principle, the plug calorimeters [**?**] are similar to the central ones, but they use more modern technology. The tower geometry is more complicated in the plug, but the 15° wedge pattern is respected. The plug electromagnetic calorimeter (PEM) has lead absorber and scintillating tile read out with

wavelength shifting fibers. An electron traversing the PEM sees 23.2 radiation lengths of material. The energy resolution for high-energy electrons and photons is $\frac{\sigma(E)}{E} = \frac{14.4\%}{\sqrt{E}} \oplus 0.7\%$. There is a shower maximum detector (PES), whose scintillating strips measure the position of electron and photon showers. The plug hadronic calorimeter (PHA) has alternating layers of iron and scintillating tile, for a total of 6.8 interaction lengths.

Muon identification is performed by banks of single-wire drift cells four layers deep. The central muon detector (CMU) [**?**] is located directly behind the hadronic calorimeter in a limited portion of the central region ($|\eta| < 0.6$). The central muon upgrade (CMP) adds additional coverage in the central region and reduces background with an additional 60 cm of steel shielding, corresponding to 2.4 interaction lengths at 90^o. The central muon extension (CMX) covers the region $0.6 < |\eta| < 1.0$, and contains eight layers of drift tubes, with the average muon passing through six.

A three-level trigger system is used to select interesting events to be recorded to tape at $\sim$ 60 Hz from the bunch crossing rate of 1.7 MHz. This analysis uses data from triggers based on high-p_T leptons, which come from the leptonically decaying W in the event. The first two trigger levels perform limited reconstruction using dedicated hardware, including the eXtremely Fast Tracker (XFT), which reconstructs r-ϕ tracks from the COT with a momentum resolution of better than $2\%/p_T[\mathrm{GeV}/c]$. The electron trigger requires a coincidence of an XFT track with an electromagnetic cluster in the central calorimeter, while the muon trigger requires that an XFT track point toward a set of hits in the muon chambers. The third level is a software trigger that performs full event reconstruction. Electron and muon triggers at the third level require fully reconstructed objects as described below, but with looser cuts.

This analysis relies heavily on the use of Monte Carlo (MC) event generation and detector simulation. Event generation is performed by HERWIG [**?**] for $t\bar{t}$ signal samples, and HERWIG, Pythia [**?**], and ALPGEN [**?**] for background and control samples. A detailed description of the CDF detector is used in a simulation that tracks the interactions of particles in each subdetector and fills data banks whose format is the same as the raw data [**?**]. The GEANT package [**?**] provides a good description of most interactions, and detailed models are developed and tuned to describe other aspects (for example, the COT ionization and drift properties) so that high-level quantities like tracking efficiency and momentum resolution from the data can be reproduced. The calorimeter simulation is

performed using a parameterized shower simulation (GFLASH [**?**]) tuned to single particle energy response and shower shapes from the data.

C. Event Selection

The selection of $t\bar{t}$ events in the lepton + jets channel begins by requiring exactly one well identified lepton candidate in events recorded by the high-p_T lepton triggers. The lepton candidate can be a central electron (CEM), or a muon observed in the CMU and CMP detectors (CMUP) or a muon observed in the CMX detector (CMX). The trigger efficiencies are high, $\sim 96\%$ for electrons and $\sim 90\%$ for muons, and show negligible p_T dependence for leptons in the final sample.

Electrons are identified by a high-momentum track in the tracking detectors matched with an energy cluster in the electromagnetic calorimeter with $E_T > 20$ GeV. Photon and hadronic fakes are reduced by requiring the ratio of calorimeter energy to track momentum to be no greater than 2 (unless $p_T > 50$ GeV/c), and by requiring the ratio of hadronic to electromagnetic energy in the calorimeter towers to be less than $0.055 + 0.00045 \cdot E_{EM}$. Isolated electrons from W decay are preferred over electrons from b or c quark semi-leptonic decay by a cut that requires the total calorimeter energy in a cone of $\Delta R = \sqrt{\Delta\phi^2 + \Delta\eta^2_{evt}} = 0.4$ around the cluster to be less than 10% of the cluster energy. Electrons are rejected if they come from photon conversions to e^+e^- pairs that have been explicitly reconstructed.

Muons are identified by a high-momentum track in the tracking detectors ($p_T > 20$ GeV/c) matched with a set of hits in the muon chambers. The calorimeter towers to which the track points must contain energy consistent with a minimum ionizing particle. An isolation cut is imposed, requiring the total calorimeter energy in a cone of $\Delta R = 0.4$ around the muon track (excluding the towers through which the muon passed) to be less than 10% of the track momentum. Cosmic ray muons are explicitly identified and rejected. A complete description of electron and muon selection, including all additional cuts used, can be found elsewhere [**?**].

A neutrino from the leptonic W boson decay is inferred when the observed momentum in the transverse plane does not balance. The missing transverse energy, $\not\!\!E_T$, is formed by projecting the energy vectors for each tower in the central, wall, and plug calorimeters into the plane transverse to the beams and summing: $\not\!\!E_T = -\|\sum_i E_T^i \mathbf{n_i}\|$, where $\mathbf{n_i}$ is the unit

vector in the transverse plane that points from the beamline to the ith calorimeter tower. The $\not\!\!E_T$ is corrected using the muon track momentum when a muon is identified in the event. For clusters of towers that have been identified as jets, the sum uses the jet energies corrected for detector response relative to the fiducial central region, for an energy scale calibration, and for the effects of multiple interactions. We require the $\not\!\!E_T$ to be at least 20 GeV.

Jets are identified by looking for clusters of energy in the calorimeter using a cone algorithm, `JETCLU`, where the cone radius is $\Delta R = 0.4$. Towers with $E_T > 1$ GeV are used as seeds, then nearby towers are added to the clusters, out to the maximum radius of 0.4. A final step of splitting and merging is performed such that in the end a tower does not contribute to more than one jet. More details about the jet clustering are available elsewhere [**?**]. Jet energies are corrected for relative detector response, energy scale calibration, and multiple interactions. See section III A 1 for further description of jet corrections.

Jets can be identified as b jets using a displaced vertex tagger, which proceeds as follows. Jets with $E_T > 15$ GeV are scanned for good-quality tracks with both COT and silicon information. When a secondary vertex can be reconstructed from at least two of those tracks, the distance between the primary and secondary vertices in the plane transverse to the beams (L_{xy}) is calculated, along with its uncertainty ($\sigma(L_{xy})$). If $L_{xy}/\sigma(L_{xy}) > 3$, the jet is considered tagged. This algorithm has an efficiency of about 55% for tagging at least one b jet in a $t\bar{t}$ event. More information concerning b tagging is available in [**?**].

We require at least four jets in the event with $|\eta| < 2.0$ in order to reconstruct the $t\bar{t}$ system. The events are separated into four subsamples based on the jet activity. These four categories of events are found to have different background content and different shapes in the reconstruction of the top mass for signal events. By treating the subsamples separately, the statistical power of the method is improved. Double-tagged (2-tag) events have two b-tagged jets in the event. These events have low background contamination, as well as excellent mass resolution, since the number of allowed jet-parton assignments is small. In this category, we require three jets with $E_T > 15$ GeV and the fourth jet with $E_T > 8$ GeV. Tight single-tagged (1-tag(T)) events have exactly one b-tagged jet in the event, and all four jets with $E_T > 15$ GeV. Loose single-tagged (1-tag(L)) events also have exactly one b tag, but the fourth jet has 8 GeV $< E_T <$ 15 GeV. These two categories have good mass resolution, but 1-tag(L) events have much higher background content than 1-tag(T) events.

TABLE I: The selection requirements for the four types of events are given. The subsamples have different background content and reconstructed mass shapes. The jet E_T requirements apply to the leading four jets in the event, but additional jets are permitted. Also shown are the expected signal to background ratios for each category.

Category		2-tag	1-tag(T)	1-tag(L)	0-tag
Jet E_T	j1–j3	$E_T > 15$	$E_T > 15$	$E_T > 15$	$E_T > 21$
cuts [GeV]	j4	$E_T > 8$	$E_T > 15$	$15 > E_T > 8$	$E_T > 21$
b tagging		2 tags	1 tag	1 tag	0 tags
Expected S:B		44:1	8.0:1	2.1:1	0.6:1
χ^2 cut		9.0	9.0	9.0	9.0

TABLE II: The number of events found and the luminosity used is given for each subsample.

Category	2-tag	1-tag(T)	1-tag(L)	0-tag
Luminosity	162 pb^{-1}	162 pb^{-1}	162 pb^{-1}	193 pb^{-1}
Number of events	2	18	8	40

Finally, 0-tag events have no b tags. Here the background contamination is quite high, so a tighter E_T cut is required: all four jets must have $E_T > 21$ GeV.

A final selection cut is based on the quality of the event mass reconstruction, detailed in section III. The value, after minimization, of the χ^2 expression giving consistency of the event with $t\bar{t}$ decay (described in equation III.4) is required to be less than 9.0, 9.0, 9.0, and 9.0 for 2-tag, 1-tag(T), 1-tag(L), and 0-tag events, respectively. This cut helps to select events with reliable mass values, discriminating against both background events and poorly recontructed signal events. The jet and χ^2 selection requirements for each of the four event types are summarized in Table I.

We find 135 $t\bar{t}$ candidates in 318 pb^{-1} of data selected for good quality in all relevant subdetectors. Events with b tags come from the 162 pb^{-1} of data with good-quality silicon detector information. In the remaining 31 pb^{-1}, b tagging is not available, so all events passing other selection cuts are treated as 0-tag events. Table II gives the number of events in each subsample.

D. Background Estimation

Wherever possible, we obtain an independent estimate of the background contamination in each subsample; adding this information as a constraint in the likelihood fit improves the result.

The amount and composition of the background contamination depends strongly on the number of jets with b tags. In the double b-tagged sample, the background contribution is negligible. In the single b-tagged sample, the dominant backgrounds are W + multijet events and non-W QCD events where the primary lepton is not from a W decay. In W + multijet events, one of the jets is either a heavy flavor jet or a light flavor jet mistagged as a heavy flavor jet. In the events with no b tag, W + multijet production dominates, and the jets are primarily light flavor since there are no b tags.

The procedures for each background type are described below in more detail, and the resulting estimates for the background composition are shown in Table III.

1. W + multijet backgrouds

Simulated samples of W + multijet backgrounds are obtained using the ALPGEN [**?**] generator, which produces multiple partons associated with a W boson using an exact leading order martrix element calculation. It is interfaced with HERWIG for parton showering and hadronization. This generator is good for high jet multiplicity events, but suffers from a large theoretical uncertainty in the normalization. Thus, the normalization for these backgrounds is taken from the data. The normalization for the tagged W + multijet contribution comes from the W + multijet events before tagging. But for 0-tag events, there is no known independent normalization; for this reason, no background constraint is used for the 0-tag sample.

The major contributions for the W + heavy flavor backgrounds, i.e. events with a b tag on a real b or c jet, come from the $Wb\bar{b}$, $Wc\bar{c}$, and Wc processes. The heavy flavor fraction for each process relative to the inclusive W + multijet process is estimated using the ALPGEN Monte Carlo samples. The estimated number of each background is then obtained by multiplying the heavy flavor fraction, the tagging efficiency, and the pretagged number of W + multijet events in the data after non-W background is subtracted. Uncertainties on

the estimate due to Q^2 scale and NLO contributions are reduced by using this technique.

Another W + multijet contribution comes from events where a light flavor jet is misidentified as a heavy flavor jet. Using generic jet data events, a per-jet mistag rate is parameterized as a function of the number of tracks, E_T, η, and ϕ of the jet, and the scalar sum of E_T for all jets with $E_T > 10$ GeV and $|\eta| < 2.4$. The mistag rate is then applied to pretag data events in the signal region to obtain the W + light flavor contribution.

2. Non-W (QCD) background

For the non-W background (QCD multijet events), a data-driven technique estimates both the pre-tagged and tagged contributions to the signal sample, because the pre-tagged sample in the W + multijet background estimation needs to be corrected for the non-W contribution. The sideband regions for the lepton isolation variable and the $\not\!\!E_T$ in the high-p_T lepton sample are used to predict the number of QCD multijet events in the signal region, assuming no correlation between the isolation and $\not\!\!E_T$.

3. Other backgrounds

There are other minor backgrounds: diboson production (WW, WZ, and ZZ) associated with jets, and single top production. We use ALPGEN Monte Carlo samples to estimate their contributions. The NLO cross section values [**?** **?**] are used for normalization.

III. MASS RECONSTRUCTION

In this section, we describe the procedure for determining the reconstructed top mass in each event and the procedure used to reconstruct the W boson decaying into the dijet final state. We then discuss the results of these reconstruction techniques. It is important to remember that the reconstructed mass is not an event-by-event measurement of the top quark mass; rather it is a quantity whose distribution in the data will be compared with simulated samples to extract the top quark mass (see section IV). The distribution of the invariant dijet mass of the W boson candidate will be used to constrain the calibration of the jet energy scale in the reconstructed events.

TABLE III: The sources and numbers of background events in the three subsamples for which background estimates exist.

Source	Expected Background		
	2-tag	1-tag(T)	1-tag(L)
W + light jets	0.05 ± 0.02	1.1 ± 0.3	0.8 ± 0.2
$Wb\bar{b}$	0.09 ± 0.03	0.6 ± 0.3	0.4 ± 0.2
$Wc\bar{c}$	0.0 ± 0.0	0.3 ± 0.1	0.1 ± 0.1
Wc	0.0 ± 0.0	0.3 ± 0.1	0.1 ± 0.1
WW/WZ	0.0 ± 0.0	0.11 ± 0.02	0.08 ± 0.01
non-W (QCD)	0.0 ± 0.0	1.2 ± 0.4	1.2 ± 0.4
Single top (S chan.)	0.0 ± 0.0	0.11 ± 0.02	0.09 ± 0.01
Single top (T chan.)	0.04 ± 0.02	0.08 ± 0.02	0.01 ± 0.01
Total	0.18 ± 0.04	3.9 ± 0.7	2.7 ± 0.6

Throughout the mass reconstruction, each event is assumed to be a $t\bar{t}$ event decaying in the lepton + jets channel, and the four leading jets are assumed to correspond to the four quarks from the top and W decays. First, the measured four-vectors for the identified physics objects in the event are corrected for known effects, and resolutions are assigned where needed. Next, a χ^2 fit is used to extract the reconstructed mass. After the procedure, each event has a particular value of reconstructed mass and a corresponding χ^2 value. Some events "fail" the mass reconstruction and are discarded when their minimized χ^2 exceeds a cut value.

A. Inputs to the mass reconstruction

The χ^2 fit takes as input the four-vectors of the various physics objects identified in the event. All known corrections are applied to the jets and lepton, and Gaussian uncertainties are established on the transverse momenta, since the p_T of each onne will be permitted to vary in the fit. The $\not\!\!E_T$ is a derived quantity, and does not have an uncertainty independent of the other measured values. The χ^2 considers instead a related fundamental quantity, the unclustered energy, which is described below.

1. Jet inputs

The jet four-vectors are the most important input to the χ^2 fit. Jets are the most numerous physics objects in the event, and they are the most poorly measured. Identifying reconstructed jets with partons from the $t\bar{t}$ decay chain has both theoretical and experimental pitfalls, and a series of corrections are made to jet energies in order to best approximate the corresponding parton energies. Measured jet energies have a large resolution, and are permitted to vary in the fit. The angles of the reconstructed jets, in contrast, are good approximations of the corresponding parton angles, so they are used without corrections and are fixed in the fit.

Jets are first corrected with a set of "generic" jet corrections, so called because they are intended to be independent of the particular process under consideration. For these corrections, when an assumption must be made about the underlying parton p_T spectrum, it is taken to be flat. Since some of the corrections are a function of jet p_T, and since the jet resolution is non-negligible, this assumption has a considerable effect on the derived correction.

These generic jet corrections scale the measured jet four-vector to account for various effects. First, a dijet balancing procedure is used to determine and correct for variations in the calorimeter response to jets as a function of η. These variations are due to different detector technology, to differing amounts of material in the tracking volume and the calorimeters, and to uninstrumented regions. In dijet balancing, events are selected with two and only two jets, one in the well understood central region ($0.2 < |\eta| < 0.6$). A correction is determined such that the transverse momentum of the other jet, as a function of its η, is equal on average to that of the central jet. This relative correction ranges from about –10% to +15%.

Another sample of events, in which a photon and a jet are the two reconstructed objects, allows an absolute measurement of the jet response, since the electromagnetic energy of the photon is well calibrated through $Z \to e^+e^-$ decays. This γ-jet balancing is used to set the overall jet energy scale to that of run I, a 6.5% correction, so that a set of sophisticated corrections for calorimeter non-linearity, derived in run I for the same central calorimeter, can be applied.

After a small correction for the extra energy deposited by multiple collisions in the same

accelerator bunch crossing, and the corrections for calorimeter non-linearity (+10% to +30%, depending on jet p_T), the jet energies correspond, on average, to the true in-cone hadronic energy for jets with a flat underlying p_T spectrum. The various sources of uncertainty in the CDF jet energy scale and simulation are described in section V A.

Next, jet corrections are applied that have been derived specifically for the $t\bar{t}$ process. There are separate corrections for light quark jets from W-boson decay (W jets) and b jets, because of their different fragmentation and decay properties. In addition, these corrections account for the shift in the mean jet energy due to the non-flat p_T spectrum of partons from $t\bar{t}$ decay. The $t\bar{t}$-specific corrections also account for the energy falling outside the jet clustering cone. W jets and b jets, which clearly have different response, are corrected using different functions, but no separate correction is attempted for b jets with identified semi-leptonic decays. The $t\bar{t}$-specific corrections also provide uncertainties on the jet energies (i.e. the measurement resolution, not systematic uncertainties). Note that, since these corrections depend on the flavor of the jet, they must be applied after a hypothesis has been selected for the assignment of the measured jets to partons from the $t\bar{t}$ decay chain.

The $t\bar{t}$-specific corrections are extracted from a large sample of HERWIG $t\bar{t}$ events in which the four leading jets in E_T are matched within $\Delta R = 0.4$ to the four generator-level partons from $t\bar{t}$ decay. The correction functions are consistent with those extracted from a large Pythia sample. The correction is defined as (the inverse of) the most probable value (MPV) of the jet response curve, as a function of p_T^{jet} and η^{jet}. The MPV is chosen, rather than the mean of the asymmetric distribution, in order to accurately correct as many jets as possible in the core of the distribution. This increases the number of events for which the correct jet-quark assignment is chosen by the fitter (see below), resulting in a narrower core for the reconstructed mass distribution (Fig. 3). A corresponding resolution is found by taking the symmetric window about the MPV of the jet response that includes 68% of the total area. Figure 2 shows the corrections and resolutions as a function of jet p_T and η.

As a final step, the jet momentum is held fixed while the jet energy is adjusted so that the jet has a mass according to its flavor hypothesis. A mass of 0.5 GeV is used for W jets, and a mass of 5.0 GeV is used for b jets. This is done for consistency with the Monte Carlo truth information used to derive the $t\bar{t}$-specific corrections.

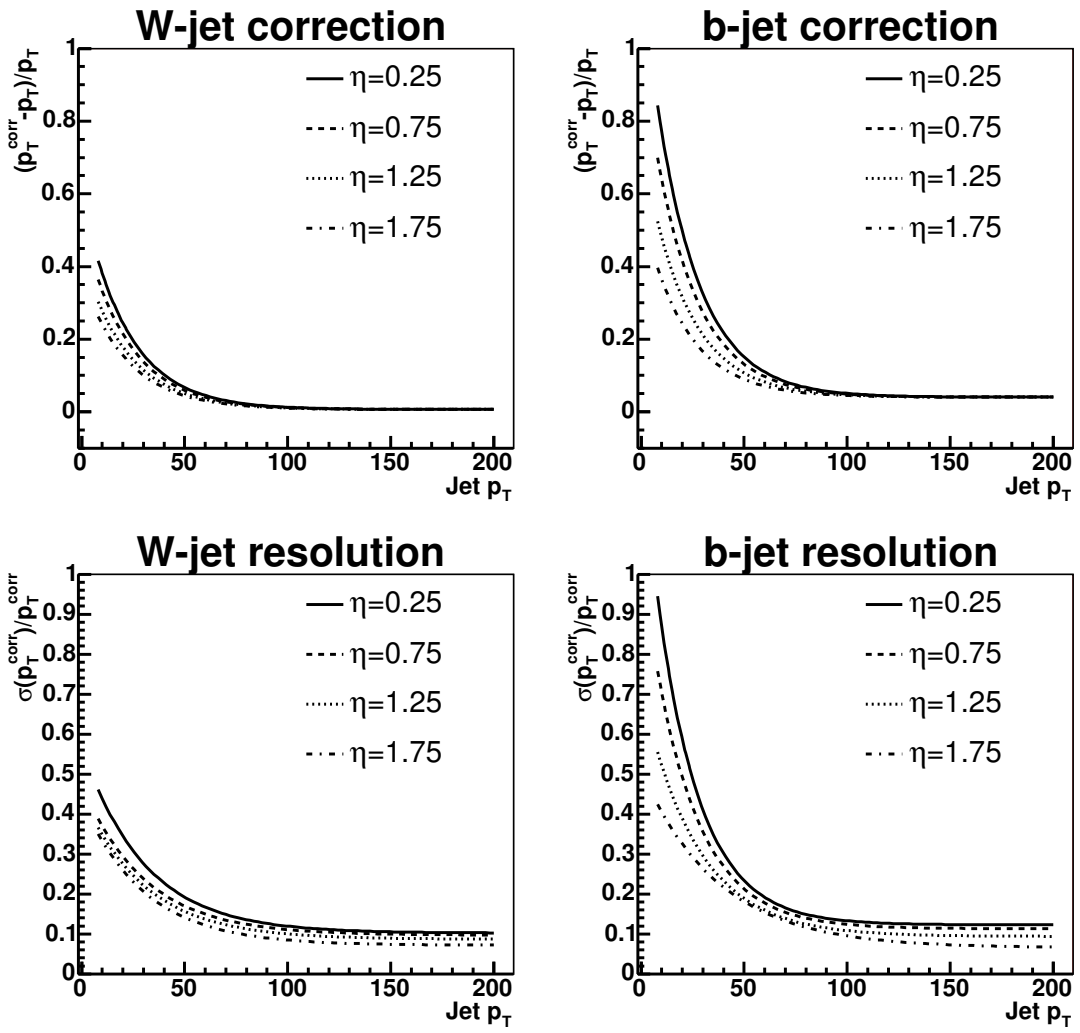

FIG. 2: The $t\bar{t}$-specific corrections are shown for W jets (left) and b jets (right) as a function of jet p_T and η. On the top is the correction factor, and on the bottom is the fractional resolution passed to the fitter.

2. Lepton Inputs

The electron four-vector has energy determined by its electromagnetic calorimeter cluster, and angles defined by the associated track. The electron energy is corrected for differences in the calorimeter response depending on where in the tower face the electron enters. The electron mass is set to zero, and the angles are taken as perfectly measured quantities. The

transverse momentum ($p_T^e = p \sin\theta$) of the electron has an uncertainty of

$$\frac{\sigma_{p_T^e}}{p_T^e} = \sqrt{\left(\frac{0.135}{\sqrt{p_T^e[\mathrm{GeV}/c]}}\right)^2 + (0.02)^2}. \qquad \text{(III.1)}$$

The muon four-vector uses the three-vector of the associated track, also with a mass of zero. Muon curvature corrections due to chamber misalignment are applied. The angles and mass are given no uncertainty; the transverse momentum has an uncertainty of

$$\frac{\sigma_{p_T^\mu}}{p_T^\mu} = 0.0011 \cdot p_T^\mu[\mathrm{GeV}/c], \qquad \text{(III.2)}$$

The electron and muon transverse momentum uncertainties are taken from studies of leptonic Z^0 decays.

3. Neutrino Inputs: Unclustered Energy

The neutrino in a $t\bar{t}$ event is not observed; its presence is inferred by an imbalance in the observed transverse momentum. Therefore, rather than treating the neutrino 4-vector as an independent input to the χ^2 fit, the measured quantities, as varied in the fit, are used to dynamically calculate the neutrino transverse momentum.

All of the transverse energy in the calorimeter (towers with $|\eta| < 3.6$) that is not associated with the primary lepton or one of the leading four jets is considered "unclustered energy." For towers clustered into a jet that has $E_T > 8$ GeV and $|\eta| < 2.0$, but that is not one of the leading four jets, the tower momenta are replaced with the jet momentum after the generic jet corrections described in section III A 1. The rest of the tower momenta are multiplied by a scale factor of 1.4, which is roughly the generic jet correction factor for 8 GeV jets. Finally, the unclustered energy includes the energy thought to enter into the leading four jets from the underlying event, and excludes the energy thought to fall outside the jet cones of the leading four jets. This avoids double-counting of energy that is included in the leading four jet energies after all corrections. Each transverse component of the unclustered energy (p_x^{UE}, p_y^{UE}) is assigned an uncertainty of $0.4\sqrt{\sum E_T^{unclus}}$, where $\sum E_T^{unclus}$ is the scalar sum of the transverse energy excluding the primary lepton and leading four jets. The uncertainty comes from studies of minimum bias events.

The unclustered energy is the observed quantity and the input to the χ^2 fit, but it is related to the missing energy through the other measured physics objects in the event, since

the $p\bar{p}$ system has $p_T = 0$. The neutrino transverse momentum p_T^ν is calculated at each step of the fit, using the fitted values of lepton, jet, and unclustered transverse energies:

$$\vec{p_T^\nu} = -\left(\vec{p_T^\ell} + \sum \vec{p_T^{jet}} + \vec{p_T^{UE}}\right) \tag{III.3}$$

Note that this quantity, used in the mass fitting procedure, is different from the missing energy described in section II C and used in event selection, where simpler calorimeter energy corrections are used.

Although this is a complicated input to the fit procedure, and other treatments of the unclustered energy and missing energy can be motivated, it has been shown that the $\not\!\!E_T$ calculation does not in fact have a large effect on the results of the χ^2 fit. Various other approaches to correcting the unclustered energy and assigning resolution were tried, and no changes had any significant effect on the top mass resolution.

As for the other components of the neutrino four-vector, the mass is fixed at zero, and the longitudinal momentum, p_z^ν, is a free (unconstrained) parameter in the fit. The initial value of p_z^ν is calculated using the initial value of the lepton four-vector and the initial p_T^ν, and assuming their mother W has its pole mass. Since these conditions yield a quadratic equation, there are in general two solutions for the p_z^ν; a separate χ^2 fit is done with each solution used as the initial value of p_z^ν. When the two fits land in different minima, we choose the one that provides the best fit using the χ^2 values as described below.

B. Event χ^2 fit

Given the inputs described above, the event-by-event fit for the reconstructed top mass proceeds as follows. MINUIT is used to minimize a χ^2 where the top mass is a free parameter. For each event, the χ^2 is minimized once for each possible way of assigning the leading four jets to the four quarks from the $t\bar{t}$ decay. Since the two W daughter jets are indistinguishable in the χ^2 expresssion, the number of permutations is $\frac{4!}{2} = 12$. In addition, there are 2 solutions for the initial value of the neutrino longitudinal momentum, so the minimization is performed a total of 24 times for each event. When b tags are present, permutations that assign a tagged jet to a light quark at parton level are rejected. In the case of single-tagged events, the number of allowed permutations is six, and for double-tagged events, it is two.

The χ^2 expression has terms for the uncertain measurements of jet, lepton, and unclus-

tered energies, as well as terms for the kinematic constraints applied to the system:

$$\begin{aligned}\chi^2 = & \sum_{i=\ell,4jets} \frac{(p_T^{i,fit} - p_T^{i,meas})^2}{\sigma_i^2} \\ & + \sum_{j=x,y} \frac{(p_j^{UE,fit} - p_j^{UE,meas})^2}{\sigma_j^2} \\ & + \frac{(M_{jj} - M_W)^2}{\Gamma_W^2} + \frac{(M_{\ell\nu} - M_W)^2}{\Gamma_W^2} \\ & + \frac{(M_{bjj} - M_t)^2}{\Gamma_t^2} + \frac{(M_{b\ell\nu} - M_t)^2}{\Gamma_t^2}. \end{aligned} \quad \text{(III.4)}$$

The first term constrains the p_T of the lepton and four leading jets to their measured values within their assigned uncertainties; the second term does the same for both transverse components of the unclustered energy. In the remaining four terms, the quantities M_{jj}, $M_{\ell\nu}$, M_{bjj}, and $M_{b\ell\nu}$ refer to the invariant mass of the sum of the four-vectors denoted in the subscripts. For example, M_{jj} is the invariant mass of the vector sum of the W daughter jets. M_W and M_t are the pole masses of the W and top quark. M_W is 80.41 GeV/c^2 [**?**], and M_t is the free parameter that will be declared the reconstructed mass after the χ^2 is minimized. The fit is initialized with $M_t = 175$ GeV/c^2. Γ_W and Γ_t are the total width of the W boson and the top quark. In order to use the χ^2 formalism, the W and top Breit-Wigner lineshapes are modeled with Gaussian distributions, using the Breit-Wigner full width at half maximum as the Gaussian sigma. Γ_W is 2.06 GeV [**?**], and Γ_t is 2.5 GeV. Thus these terms provide constraints such that the W masses come out correctly, and the t and $\bar{t}$ masses come out the same (modulo the Breit-Wigner distribution, here modeled by a Gaussian, in both cases).

The jet-parton assignment (and p_z^ν solution) with the lowest χ^2 after minimization is selected for each event. The χ^2 of this combination is denoted $\chi^2_{\rm min}$ (or just χ^2 when the context is unambiguous), and the requirement $\chi^2_{\rm min} < \chi^2_{\rm cut}$ is imposed. The χ^2 cut values given in Table I were found to give the best expected statistical uncertainty on the top mass, although the dependence on the values of the cut is not strong. So at this stage, after mass reconstruction, each event either has been rejected or can be described by a single value of this reconstructed mass variable. Indeed, the rest of the analysis can be performed with nothing more than a list of the reconstructed masses for events in various samples that have passed all selection cuts.

C. Dijet Mass and Jet Energy Scale

One of the largest systematic uncertainties in the top quark mass measurement is the jet energy scale, which relates the observed energy in the calorimeter associated with a reconstructed jet to the parent parton that created the jet. We use the W boson decay to two jets as a direct means of constraining the accuracy of the jet energy scale. We do this by comparing the observed dijet invariant mass for the W boson daughter jets with the distribution expected for a W boson decay assuming a shift in the jet energy scale.

The shift in jet energy scale is given by JES, which is the relative shift in the jet energy scale in units of the nominal uncertainty in the jet energy scale derived from the extrinsic calibration procedures. Although the jet energy scale uncertainty varies with energy, a one unit shift in the JES parameter is equivalent to an approximately 3% shift in the jet energy scale.

We reconstruct the dijet mass in the same data sample used to reconstruct the observed top quark mass, with the exception that we relax the χ^2 requirement on the jet-parton assignments under consideration, and we elect to use all of the possible jet-parton assignments in each event. The imposition of the χ^2 requirement imposes a bias in the dijet masses being considered and therefore reduces the sensitivity of the dijet mass distribution to JES. Similarly, Monte Carlo studies have shown that the sensitivity of the dijet mass distribution to the JES parameter is maximized by considering all dijet mass combinations possible in each event. We note that the number of possible combinations range from 1 (for double b-tagged events) to 6 (for 0 tagged events).

We simultaneously fit the reconstructed top quark mass distributions and the dijet mass distributions to the Monte Carlo predictions, which are parametrized as a function of the true top quark mass and JES.

D. Mass reconstruction results

Typical reconstructed mass distributions for signal Monte Carlo ($M_{top} = 175$ GeV/c^2) are shown for the four event categories as the green histograms in Fig. 3. Each event in the sample that passes both event selection and the χ^2 cut contributes exactly one entry to these histograms. As expected, the distributions peak near the generated mass of 175 GeV/c^2, but

an exact correspondence between the generated mass and, say, the mean of the reconstructed mass is neither sought nor expected. Differences can arise when ISR/FSR jets are selected instead of the $t\bar{t}$ decay products; even with the correct jets, the fit may choose the wrong jet-parton assignment. In particular, the broader shape, beneath the relatively sharp peak at 175 GeV/c^2, comprises events where an incorrect permutation has been chosen in the fit. The red histograms in the same figure show the reconstructed mass distributions for events where the four leading jets correspond to the four partons from $t\bar{t}$ decay, and where the correct jet-parton assigment is chosen by the fit. These histograms have much smaller tails than the overall distributions.

Some results of the mass reconstruction on Monte Carlo $t\bar{t}$ signal ($M_{top} = 175$ GeV/c^2) and background samples are given in Table IV. The four subsamples have significantly different shapes for $t\bar{t}$ signal, as evidenced by their reconstructed mass mean and RMS values. The χ^2 cut efficiency is lowest for 2-tag events, especially in the background, because there are fewer allowed jet-parton assignments and thus fewer chances to pass the χ^2 cut. The means of the background reconstructed mass distributions are primarily driven by the jet cuts (see Table I).

The reconstructed mass distribution for the 135 events found in the data can be seen in Fig. 4, separated into the four subsamples. These events consist of both $t\bar{t}$ signal and background events. Figure 5 shows the distribution of χ^2 values in data and simulated events, where the distribution from simulation contains the expected mixture of signal and background events. The distributions agree nicely, indicating that kinematic quantities and resolutions are well simulated.

The corresponding dijet mass distributions for the W boson reconstruction are shown in Fig. 6 for the four subsamples. One sees a clear W boson mass signal, with a peak near the nominal W boson mass of 80.32$\pm$?? GeV/c^2. The peak becomes more evident with increasing numbers of b-tagged jets in the event, a consequence of the decreasing number of combinations for W boson jet daughters.

IV. TOP MASS FITTING

The two-dimensional distribution of reconstructed top quark mass and dijet invariant mass for a particular Monte Carlo sample is referred to as a template. The distribution of the

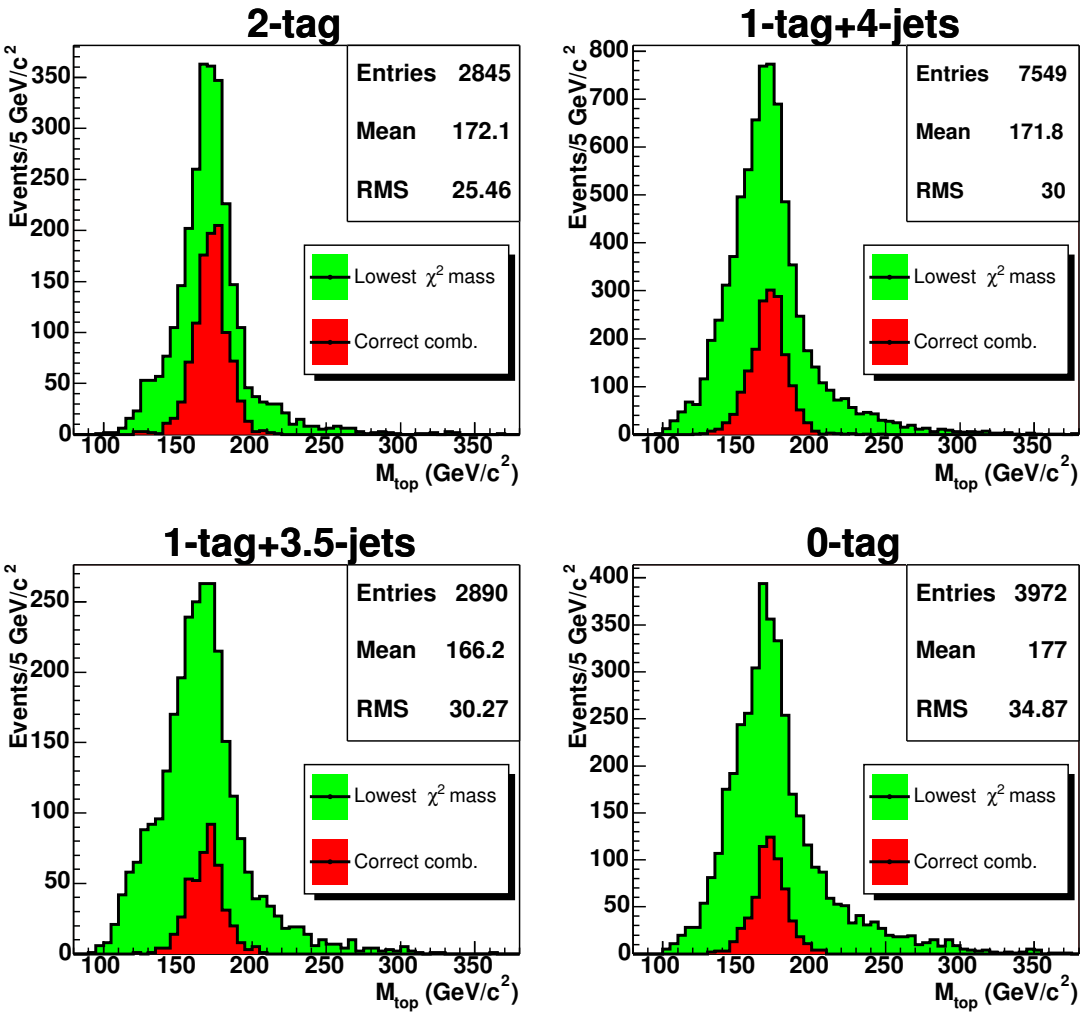

FIG. 3: In green, the reconstructed mass distribution for the 175 GeV/c^2 HERWIG $t\bar{t}$ sample. Overlaid in red is the reconstructed mass distribution for the correct parton-jet assignment, in the subset of events for which the leading four jets are matched (within $\Delta R = 0.4$) to the four partons from the $t\bar{t}$ decay. Distributions are shown for 2-tag (upper left), 1-tag(T) (upper right), 1-tag(L) (lower left), and 0-tag (lower right) events.

reconstructed mass in data events will be compared to Monte Carlo signal and background templates to extract the measured top quark mass and the jet energy scale. First, probability density functions (p.d.f.'s) of the reconstructed masses are determined from the templates for signal and background events; the signal p.d.f.'s depend on the true top quark mass and jet energy scale. We perform an unbinned likelihood fit to extract the best value of the top quark mass and jet energy scale to describe the data. At the end of this section, we describe

TABLE IV: Monte Carlo samples of $t\bar{t}$ signal and of background processes with the expected relative weights are run through the χ^2 mass fitter. For signal and background in each of the four event categories, the table shows the efficiency of the χ^2 cut and the mean and RMS of the resulting reconstructed mass distribution.

Sample	χ^2 cut	M_{reco} [GeV]	
Description	eff.	Mean	RMS
Signal ($M_{top} = 175$ GeV/c^2)			
2-tag	0.67	172.1	25.5
1-tag(T)	0.83	171.8	30.1
1-tag(L)	0.86	166.2	30.3
0-tag	0.92	177.0	34.9
Background			
2-tag	0.37	164.9	36.1
1-tag(T)	0.70	165.0	40.6
1-tag(L)	0.70	153.6	36.1
0-tag	0.85	180.9	45.7

a number of checks of the method using simulated events.

A. Parameterization of Signal and Background Shapes

Since templates are available only at discrete values of true top quark mass and jet energy scale, the signal reconstructed mass distributions are parameterized by a flexible functional form as a function of true top quark mass and jet energy scale in order to smooth the distributions and interpolate between the mass points. For background events, there is no dependence on top quark mass or jet energy scale; a single p.d.f. is used to describe the background reconstructed mass shape.

In principle, the jet energy scale may change the shape of the background templates. However, we have determined from studies of the background that the shape of the background template is insensitive to the jet energy scale. Rather, the overall rate of background events does show some sensitivity to the jet energy response, and this uncertainty is incor-

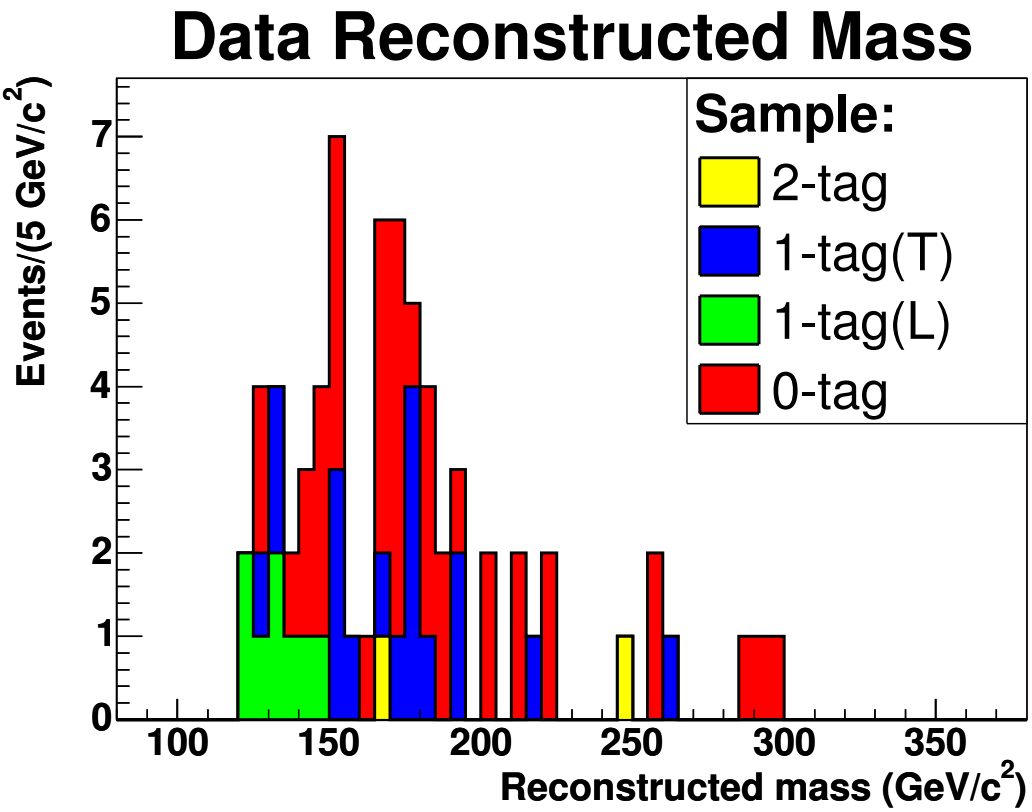

FIG. 4: The reconstructed mass for events in the data is shown, with events from the four sub-samples represented by histograms in yellow (2-tag, 2 events), blue (1-tag(T), 18 events), green (1-tag(L), 8 events), and red (0-tag, 40 events).

porated, where appropriate, into the uncertainty in the rate of background events in the sample.

1. *Signal shape parameterization*

Signal mass templates are produced using sets of Monte Carlo samples with the input top quark mass at 2.5–5 GeV/c^2 intervals from 130 GeV/c^2 to 230 GeV/c^2 and the jet energy scale varying from -3.0 to +3.0 in steps of 0.5. An example of the template shape from each event category is given in Fig. 3. Table V shows the evolution of the template mean, most probable value, and RMS as a function of top quark mass using selected generated mass samples and jet energy scales.

We derive from these distributions parametrized templates that are a smoothly varying

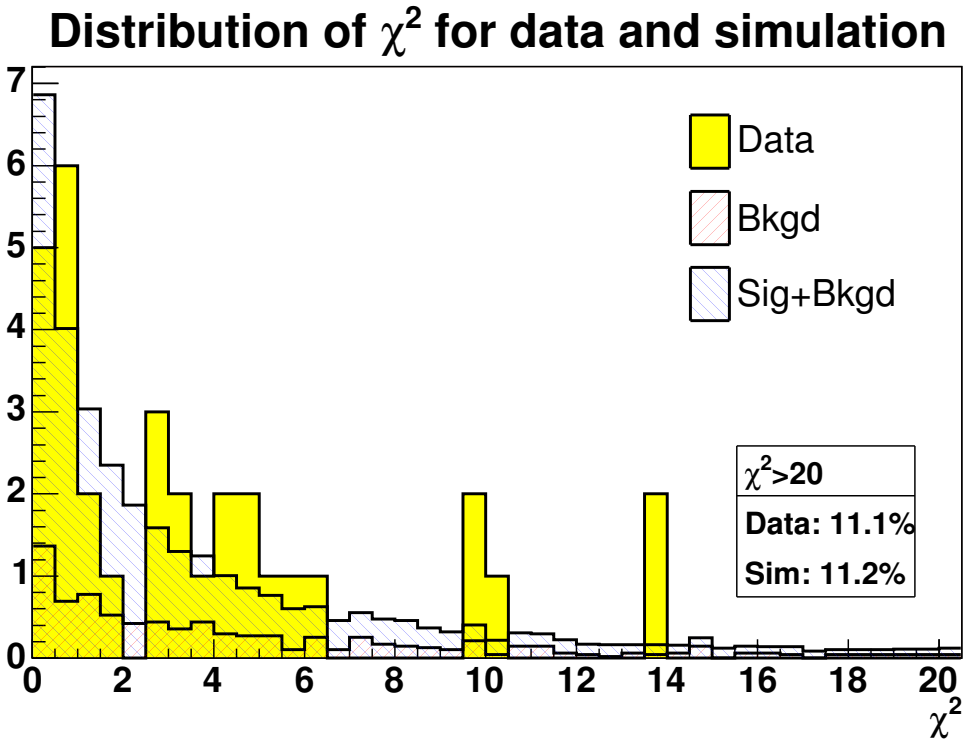

FIG. 5: The χ^2 distribution is shown for data events and for signal and background simulated events in the expected ratio. In this plot only events with at least one b tag are used.

FIG. 6: The reconstructed dijet mass for events in the data is shown, with events from the four subsamples represented by histograms in yellow (2-tag, 2 events), blue (1-tag(T), 18 events), green (1-tag(L), 8 events), and red (0-tag, 40 events).

function of true top quark mass and jet energy scale. An arbitrary parameterization is used for the probability to observe a particular reconstructed top quark mass given the true top quark mass and jet energy scale. For a given true top quark mass, the parameterization consists of two Gaussians—intended to account for the well measured events—plus the integrand of the Gamma function—intended to account for events where the incorrect combination is chosen, or where the four leading jets do not match the four partons from the $t\bar{t}$ decay. The 9 parameters necessary to specify this combination of functions are themselves assumed to depend linearly on the true top quark mass and jet energy scale, so that the full set of templates is specified by 27 parameters. This assumed functional form is certainly arbitrary as well, but works well in the limited range of top quark masses and jet energy scales considered; assuming quadratic dependence does not improve the fit. Thus

TABLE V: The evolution of the template parameters is demonstrated using selected signal Monte Carlo samples with generated top quark mass of 145 GeV/c^2, 165 GeV/c^2, 185 GeV/c^2, and 205 GeV/c^2, with jet energy scales of -1.0, 0.0 and +1.0. The mean, most probable value (MPV), and RMS of the templates are given for each subsample in each generated mass.

	M_{top}^{gen}	2-tag	1-tag(T)	1-tag(L)	0-tag
Template	145	150.5	154.7	147.3	163.1
Mean	165	165.6	167.3	160.7	172.9
[GeV/c^2]	185	178.5	180.5	172.2	183.9
	205	193.2	192.6	185.1	194.6
Template	145	144.9	144.0	141.6	147.7
MPV	165	162.0	160.0	156.6	159.6
[GeV/c^2]	185	178.9	178.6	176.3	179.0
	205	199.8	198.0	191.0	198.4
Template	145	22.8	30.4	25.9	34.5
RMS	165	25.4	30.6	28.4	36.7
[GeV/c^2]	185	26.7	33.5	29.3	35.2
	205	28.3	33.1	33.2	37.0

the parameterization is as follows:

$$\begin{aligned} P_{sig}(m;M,\mathrm{JES}) \;=\; & \alpha_7 \cdot \frac{\alpha_2^{1+\alpha_1}}{\Gamma(1+\alpha_1)} \cdot (m-\alpha_0)^{\alpha_1} e^{-\alpha_2(m-\alpha_0)} \\ & +\alpha_8 \cdot \frac{1}{\alpha_4\sqrt{2\pi}} \cdot e^{\frac{-(m-\alpha_3)^2}{2\alpha_4^2}} \\ & +(1-\alpha_7-\alpha_8) \cdot \frac{1}{\alpha_6\sqrt{2\pi}} \cdot e^{\frac{-(m-\alpha_5)^2}{2\alpha_6^2}}; \end{aligned} \tag{IV.1}$$

where

$$\alpha_i = p_i + p_{i+9} \cdot (M-175) + p_{i+18} \cdot (\mathrm{JES}),$$

The variable m in GeV/c^2 refers to the reconstructed top quark mass, M in GeV/c^2 refers to the true top quark mass, and JES refers to the true shift in the jet energy scale from that determined from our calibrations. These template parametrizations are normalized so that, for a given true top quark mass M and jet energy scale JES, the integral over

all reconstructed top quark masses m is unity. Similar parametrizations are developed for templates as a function of the dijet invariant mass M_{jj}.

A binned likelihood fit is used to extract the 27 parameter values. The χ^2 is calculated between the MC samples and the prediction from the fit, after rebinning to ensure that each bin has at least five predicted events. The resulting χ^2 values are given in Table VI, along with the number of degrees of freedom. Although the corresponding probabilities are quite small, due to the large statistics of the templates, the fit matches the template shapes quite well. This is demonstrated in Fig. 7, where four signal templates at varying generated masses are shown overlaid with the fitted parameterization evaluated at each true mass. In this figure can also be seen the changing shape of the reconstructed mass templates as a function of true mass. We show in Fig. 8 the similar distributions for the M_{jj} templates with varying jet energy scale. One sees that the location of the W boson peak is sensitive to the jet energy scale.

2. Background shape parameterization

Monte Carlo simulations of the various processes listed in section II D are used to model the reconstructed observed top quark mass shape and dijet mass shape for background processes. When possible, due to limited computing resources, a single large-statistics sample is used to represent several background processes.

For the tagged backgrounds, the W + heavy flavor processes ($Wb\bar{b}$, $Wc\bar{c}$, Wc) all have similar reconstructed mass shapes, as shown in Fig. 10, and thus are all modeled with a high-statistics $Wb\bar{b}$ simulated sample. WW and WZ events, a negligible contribution to the total expected background, are also included in this category. The shapes for the three subsamples with tagged events are found by reconstructing the simulated events exactly as is done for the data and signal Monte Carlo. Similarly, the simulated s- and t-channel single top quark events are used to obtain corresponding mass templates.

The mass templates for the W + jets backgrounds in the tagged subsamples, i.e. "mistags," are not obtained using the Monte Carlo b tagging, which is not expected to model well the rate or kinematic dependences of fake tags. Instead, a mistag matrix, derived from the data, is used to give the probability for a jet to be falsely tagged as a function of its E_T, ϕ, η, number of tracks, and the ΣE_T for all jets in the event. Then for each simulated

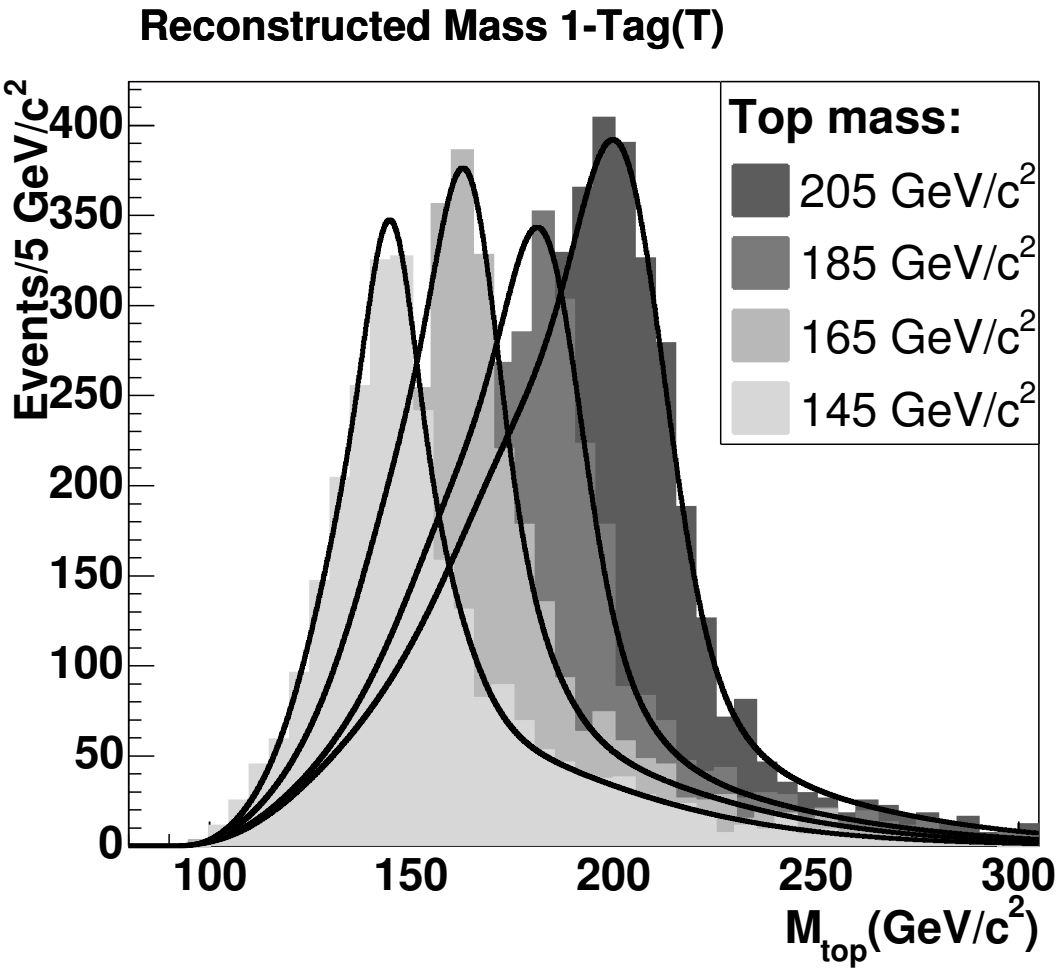

FIG. 7: Four signal templates are shown with top quark masses ranging from 145 GeV/c^2 to 205 GeV/c^2, with JES set to 0. Overlaid are the fitted parameterizations at each generated mass, taken from the full parameterization given in Eq. IV.1.

FIG. 8: Four M_{jj} signal templates are shown with various JES values and the true top quark mass set to 180 GeV/c^2. Overlaid are the fitted parameterizations at each generated mass, taken from the full parameterization given in Eq. IV.1.

event (W + 4 partons, generated by ALPGEN and showered by Pythia), every possible tag configuration on the leading four jets is considered. For every tag configuration, the best assignment of jets to partons is determined respecting the assumed tags, and the appropriate mass template is filled with a weight corresponding to the probability of observing that set of tags. The result is a weighted template for the mistag backgrounds.

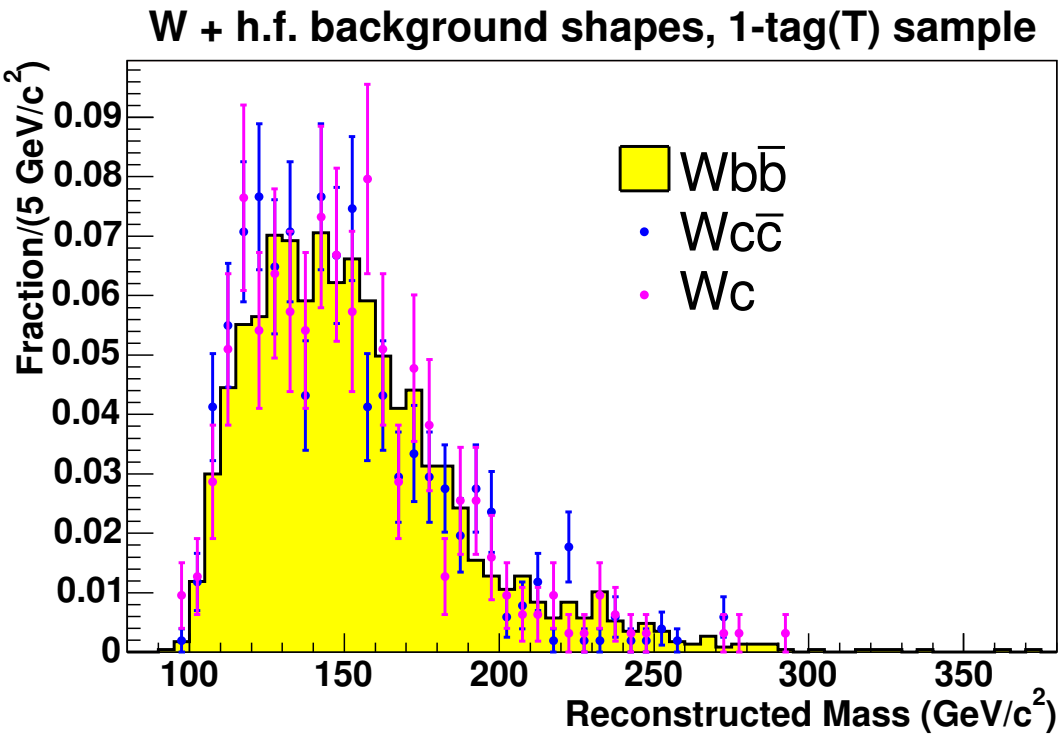

FIG. 9: The templates for $Wc\bar{c}$ and Wc background processes are compared to the high-statistics $Wb\bar{b}$ template for all tagged events. The agreement is good in both cases, so the $Wb\bar{b}$ template is used to represent all W + h.f. processes.

The backgrounds that are least amenable to Monte Carlo modelling arise from QCD background events, i.e. events with no real W to produce the isolated lepton and $\not\!\!E_T$. These events are difficult to simulate, but can be studied by selecting events in the data with non-isolated leptons, which are enriched in this type of background, but kinematically similar to events chosen in the default selection. Within the limited statistics available, Fig. 11 and Fig. **??** show that the reconstructed mass distributions of the QCD-enriched events are consistent with that of W + jets events. On the left in Fig. **??**, the 0-tag events are compared, and on the right, the combined tagged events are compared with the combined mistag template. The shapes appear to be very similar. A KS test gives a probability of 99% for the 0-tag events, and 6.5% for the tagged events. Given these similarities, the W + jets reconstructed mass templates are used also for the expected contributions from QCD for both the reconstructed top quark mass and the dijet invariant mass.

The background for the 0-tag subsample is treated separately from the others. The

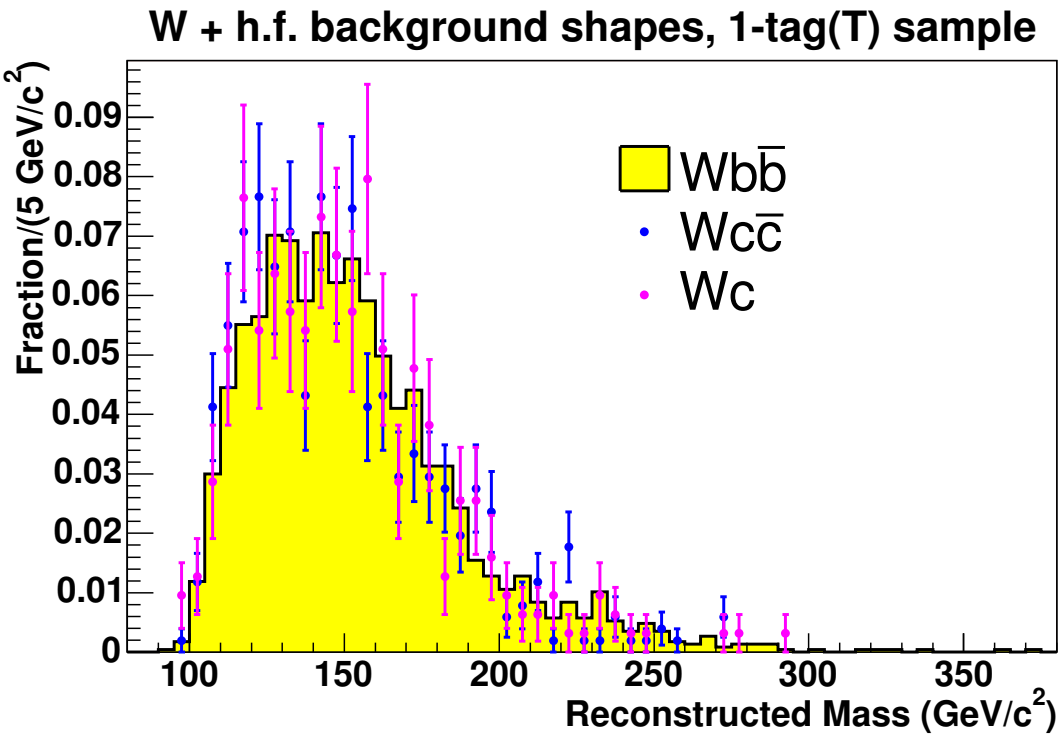

FIG. 10: The templates for $Wc\bar{c}$ and Wc background processes are compared to the high-statistics $Wb\bar{b}$ template for all tagged events. The agreement is good in both cases, so the $Wb\bar{b}$ template is used to represent all W + h.f. processes.

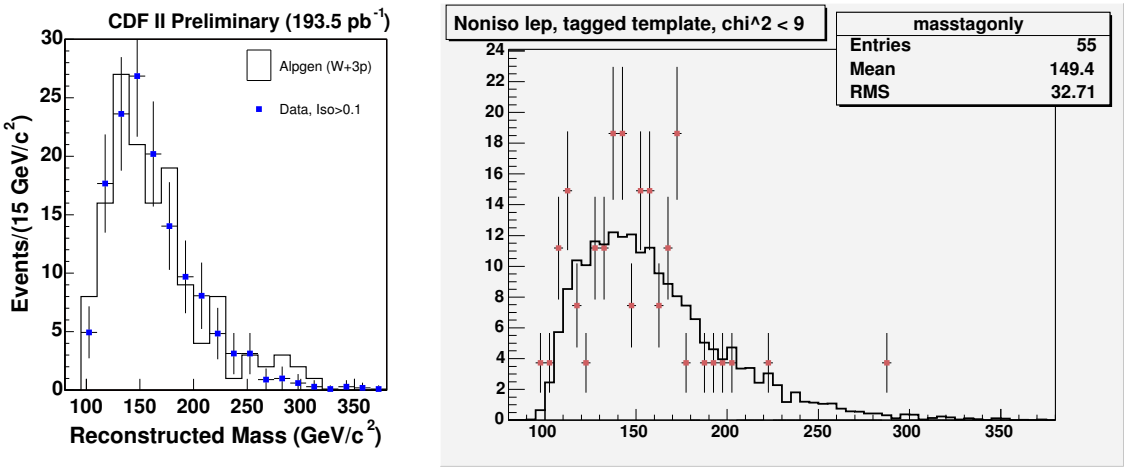

FIG. 11: W + jets background templates (histograms) and data events with non-isolated leptons (points) are compared. The latter are enriched in non-W (QCD) background. At left, the points are 0-tag events. At right, the points are the three tagged categories combined to improve statistics.

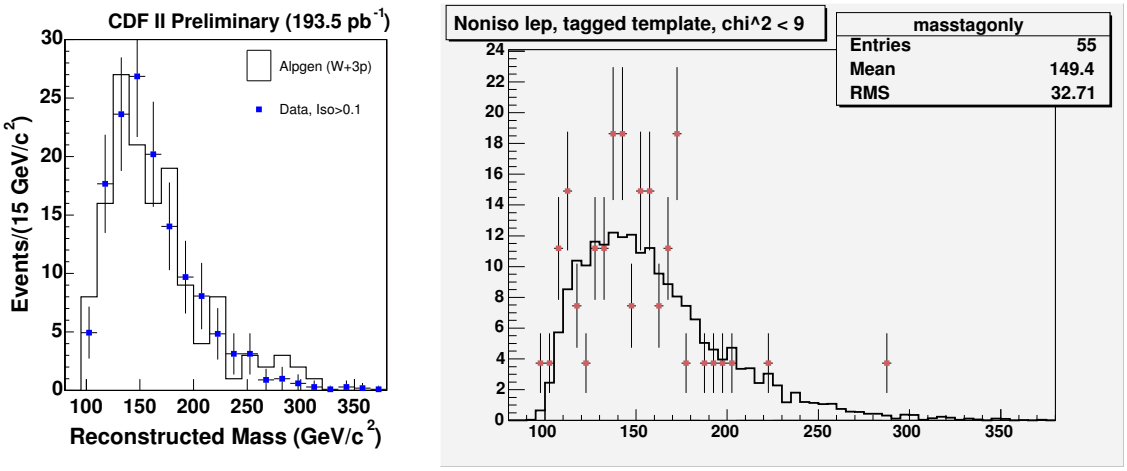

FIG. 12: W + jets background templates (histograms) and data events with non-isolated leptons (points) are compared. The latter are enriched in non-W (QCD) background. At left, the points are 0-tag events. At right, the points are the three tagged categories combined to improve statistics.

dominant process is W + jets, with a smaller ($\sim$ 20%) contribution from non-W (QCD) events. As above, the reconstructed mass shape for events in the data with non-isolated leptons matches well the simulated W + jets template. Thus the entire 0-tag background shape comes from W + 3 parton Monte Carlo events, simulated by ALPGEN and showered by Pythia.

We do not allow each background contribution to vary independently in the final likelihood fit. Instead, for each subsample, the background processes are combined in their expected ratios according to Table III. A single function is fit to the combined background for each subsample and is used to describe the background shape in the final likelihood fit (section IV B). The overall background normalization for each subsample is then permitted to vary in the fit.

We determine the p.d.f.'s for the background reconstructed mass templates using a parameterization similar in spirit to that of the signal, but simpler in form. First, there is no dependence on top quark mass. Second, no narrow Gaussian peak is expected, so the full shape is modeled by the integrand of the Gamma function. Specifically,

$$P_{bg}(m) = \frac{p_2^{1+p_1}}{\Gamma(1+p_1)} \cdot (m-p_0)^{p_1} e^{-p_2(m-p_0)}, \qquad \text{(IV.2)}$$

where m in GeV/c^2 is the reconstructed top quark mass. In the case of the 0-tag background

TABLE VI: The χ^2 and number of degrees of freedom are given for the signal parameterization fits in each of the four subsamples.

2-tag	1-tag(T)	1-tag(L)	0-tag
χ^2/n.d.o.f. for reconstructed top quark mass (Eq. IV.1)			
13977/13081	18736/17052	14209/13444	18791/16752
χ^2/n.d.o.f. for dijet mass (Eq. IV.1)			
19541/17000	29410/25732	23506/19827	38315/30510

events, a slightly more sophisticated function is used to achieve a good fit:

$$\begin{aligned} P_{bg0}(m) &= p_6 \frac{p_2^{1+p_1}}{\Gamma(1+p_1)} \cdot (m-p_0)^{p_1} e^{-p_2(m-p_0)} \\ &+ (1-p_6) \frac{p_5^{1+p_4}}{\Gamma(1+p_4)} \cdot (m-p_3)^{p_4} e^{-p_5(m-p_3)}. \end{aligned} \tag{IV.3}$$

After rebinning so that each bin has at least five predicted events, the χ^2 for the fits show reasonable agreement (Table VI). The final background templates for the reconstructed top quark mass and dijet mass for the four subsamples are shown in Fig. 13 and Fig. **??**, respectively.

B. Likelihood Fit for Top Quark Mass

The reconstructed mass distributions from data are simultaneously compared to the templates from signal and background sources using an unbinned extended likelihood fit. The likelihood involves parameters for the expectation values of the number of signal and background events in each subsample, and for the true top quark pole mass and jet energy scale. For each subsample, the likelihood is given by:

$$\begin{aligned} \mathcal{L} &= \mathcal{L}_{shape}^{m_t} \times \mathcal{L}_{shape}^{m_{jj}} \times \mathcal{L}_{sig} \times \mathcal{L}_{bg}; \\ \mathcal{L}_{shape}^{m_t} &= \frac{e^{-(n_s+n_b)}(n_s+n_b)^N}{N!} \times \\ &\quad \prod_{i=1}^{N} \frac{n_s P_{sig}(m_i; \mathrm{M_{top}}) + n_b P_{bg}(m_i)}{n_s + n_b}; \\ \mathcal{L}_{sig} &= e^{-\frac{(n_s - n_s^{exp})^2}{2\sigma_{n_s}^2}}; \\ \mathcal{L}_{bg} &= e^{-\frac{(n_b - n_b^{exp})^2}{2\sigma_{n_b}^2}}. \end{aligned} \tag{IV.4}$$

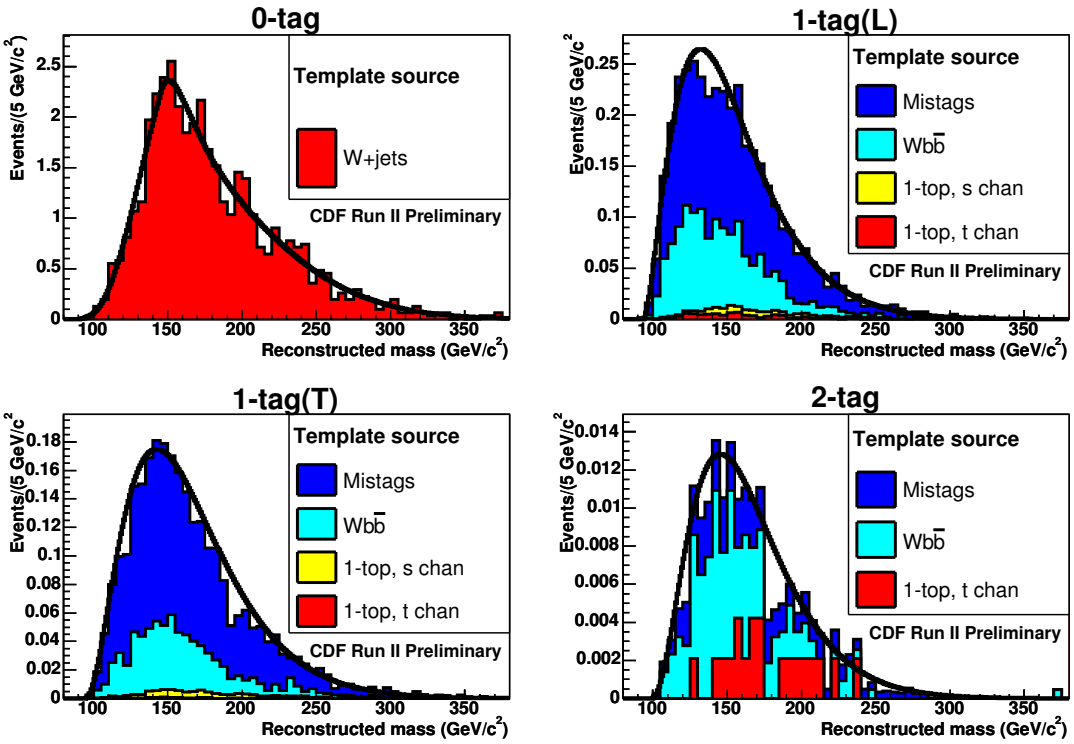

FIG. 13: Reconstructed mass distributions of the combined backgrounds in each subsample. The contributions from different background templates are shown stacked; overlaid are the fitted curves (see Eq. IV.2).

FIG. 14: Reconstructed dijet mass distributions of the combined backgrounds in each subsample. The contributions from different background templates are shown stacked; overlaid are the fitted curves (see Eq. IV.2).

The most information on the true top quark mass is provided by the products in $\mathcal{L}_{shape}^{m_t}$, the ith term of which gives the probability of observing the ith data event with reconstructed mass m_i, given the background template, $P_{bg}(m_i)$, and the signal template with a true top quark mass of $\mathrm{M_{top}}$ and energy scale shift JES, $P_{sig}(m_i; \mathrm{M_{top}}, \mathrm{JES})$. The third term represents the information arising from the number of signal and background events in the top quark mass and dijet mass samples, which are correlated. We denote the number of expected signal and background events in the $W \to jj$ sample, n_s^W and n_b^W, respectively. The expected numbers of signal and background events in the m_t sample are given by $\epsilon_s n_s^W$ and $\epsilon_b n_b^W$, respectively, where the two parameters ϵ_s and ϵ_b represent the efficiency of the χ^2 cut for signal and background events. The efficiencies for signal range from 0.65 to

0.92 while the efficiencies for background range from 0.44 to 0.83. The third term in the likelihood, $\mathcal{L}_{nev}$, expresses the likelihood associated with observing r_W and r_t events in the two samples given the expected number of events and the expected efficiencies. The first sum expresses the Poisson probability to observe r_s^W signal and r_b^W background events given Poisson means of n_s^W and n_b^W, respectively. The sum in the third term is over the sum of those signal and background events that equal the observed number of events in the m_{jj} sample: $r_s^W + r_b^W = r^W$. For each pair in this sum, we then include the binomial probability to observe r_s^t signal events and r_b^t background events in the m_t sample given the numbers of observed events in the mjj sample and the χ^2_{min} cut efficiencies. The second sum in the $\mathcal{L}_{nev}$ is over the pairs of signal and background events in the m_t sample that equal the observed number of events: $r_s^t + r_b^t = r^t$.

When independent estimates of background are available, the background normalizations are constrained in the likelihood fit by Gaussian terms with the form of $\mathcal{L}_{bg}$. The background normalizations are constrained for the 2-tag, 1-tag(T), and 1-tag(L) samples, and the signal normalization is constrained for the 0-tag sample. Both n_s and n_b are required to be greater than zero.

Independent detector calibrations and studies of other processes allow us to independently determine the jet energy scale JES, and this information is used in the reconstruction of the data events and in the determination of the signal templates. We include in the likelihood fit the knowledge of this independent jet energy calibration through a likelihood defined by a Gaussian constraint

$$\mathcal{L}_{\rm JES} = e^{-\frac{({\rm JES}-{\rm JES}^{exp})^2}{2\sigma^2_{\rm JES}}} \tag{IV.5}$$

$$= e^{-\frac{{\rm JES}^2}{2}}, \tag{IV.6}$$

where the simplication arises because by definition the measured shift in energy scale, ${\rm JES}^{exp} = 0$ and the uncertainty $\sigma_{\rm JES} = 1.0$.

The total likelihood is given by the product of the likelihoods for the four subsamples and the jet energy scale constraint

$$\mathcal{L} = \mathcal{L}_{2-tag} \times \mathcal{L}_{1-tag(T)} \times \mathcal{L}_{1-tag(L)} \times \mathcal{L}_{0-tag} \times \mathcal{L}_{\rm JES}. \tag{IV.7}$$

The top quark pole mass $\rm M_{top}$ and jet energy scale JES are shared between the four likelihoods and are free parameters in the fit. The likelihood is maximized with respect to all

ten parameters (n_s and n_b for four subsamples, JES and M_{top}) using the MINUIT package. A likelihood curve as a function of M_{top} is found by maximizing the likelihood with respect to all other parameters for a series of fixed M_{top}. The statistical uncertainty from the fit procedure is taken from the points M^+_{top} and M^-_{top} where the log-likelihood changes by $+1/2$ unit from its minimum. The positive and negative uncertainties are then scaled to achieve 68.3% coverage of the true mass value as described below in section IV C.

We can also obtain a refinement in our measurement of the jet energy scale by assuming a fixed M_{top} and calculating confidence intervals for JES. This provides a direct test of the consistency of our independent jet energy scale determination with the M_{jj} distributions observed in the mass candidate sample.

C. Method Check

The method described above is checked for any possible systematic biases by running large numbers of "pseudoexperiments," where we create, using Monte Carlo signal and background events, samples of signal and background events with an assumed value of the true top quark mass and jet energy scale and with the same statistical properties as our observed sample. We then perform likelihood fits to each pseudoexperiment and characterize the accuracy of the technique in determining the true values.

For each pseudoexperiment, first the number of signal and background events is determined, then a reconstructed top quark mass and dijet mass are generated for each event. The number of background events in each subsample is Poisson fluctuated around the central value given in Table III. The number of signal events is Poisson fluctuated around the number observed in the data, minus the central value for the background expectation, for each subsample. For each event, a reconstructed mass is selected at random from the template histogram corresponding to signal or background processes. The resulting list of reconstructed masses is fit using exactly the same machinery as will be used on the data, described in section IV B. We note the correct statistical correlations between the M_{jj} and the top quark mass sample are modelled in this procedure.

For each pseudoexperiment, the likelihood fit provides a measured top quark mass M_{top} and jet energy scale JES, as well as positive and negative errors ($\delta^+_{M_{top}}$ and $\delta^-_{M_{top}}$) from the $\Delta \ln L = +1/2$ procedure. The pulls of the measurement are checked using the symmetrized

errors, where the uncertainty on the top quark mass is taken to be $.5(\delta^+_{\mathrm{M_{top}}} + \delta^-_{\mathrm{M_{top}}})$. A pull distribution is generated for each of 12 input values for the top quark mass, keeping JES fixed to zero, where 10,000 pseudoexperiments are generated for each input mass value, and each pull distribution is fitted using a Gaussian function. The mean and sigma of the fitted functions are shown in Fig. 15 and Fig. 16, respectively. The pull means show no overall bias, but the widths are slightly larger than one. We determine a similar set of pull distributions for the JES parameter, keeping the true top quark mass fixed to 180 GeV/c^2. The results are shown in Fig. 17 and Fig. 18, and demonstrate that the technique has no overall bias.

The inflation of the pull widths is due to the low statistics of the event sample. For a small number of events, and for templates such as the ones described in section IV A, the resulting likelihood curve is typically non-Gaussian, and in fact, typically shallower than Gaussian. This likelihood shape, using any definition of the measurement error, in turn provokes large non-Gaussian tails in a pull distribution, which lead to a fitted pull width greater than one. The pull distributions become more Gaussian (with width one) as pseudoexperiments with more events are performed. With ten times the statistics, the pull widths are consistent with one.

For the current low-statistics data sample, the quoted measurement with uncertainties is designed to include the true mass value 68.3% of the time by scaling the errors taken from $\Delta \ln L = +1/2$. The scale factor is that necessary so that 68.3% of an ensemble of pseudoexperiments include the simulated top quark mass. The factor is determined using pseudoexperiments for an input mass near the measured value, and uses $\delta^+_{\mathrm{M_{top}}}$ and $\delta^-_{\mathrm{M_{top}}}$ rather than a symmetrized error.

The statistical errors from the ensembles of pseudoexperiments at various top quark masses are depicted in Fig. 19. The mean, median, 68th percentile, and 90th percentile of the symmetrized error are plotted as a function of the input top quark mass. The expected statistical error increases with the top quark mass, but the fractional uncertainty decreases. No scaling of the errors is performed in this plot.

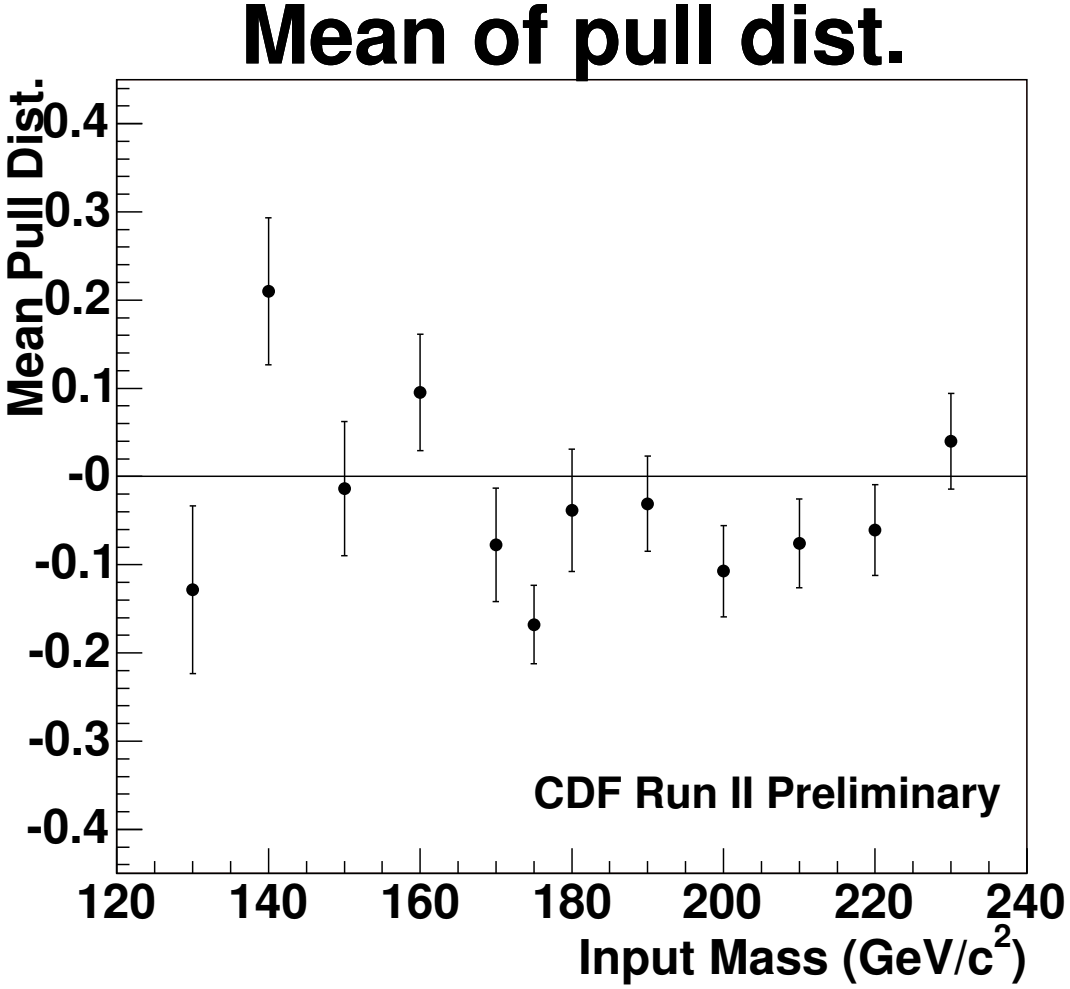

FIG. 15: The Gaussian mean of pull distributions from 10,000 pseudoexperiments as a function of true top quark mass. The error bars come mostly from the limited statistics of the Monte Carlo sample from which the pseudodata is taken.

D. Results on the Data

1. *Subsample Likelihood Curves*

The likelihood fit is first performed on each subsample separately. For a series of top masses between 110 GeV/c^2 and 250 GeV/c^2, the mass parameter is fixed, while the likelihood is maximized with respect to the remaining parameters (n_s and n_b) using MINUIT. The resulting negative log-likelihood curves as a function of top mass are shown in Fig. 20.

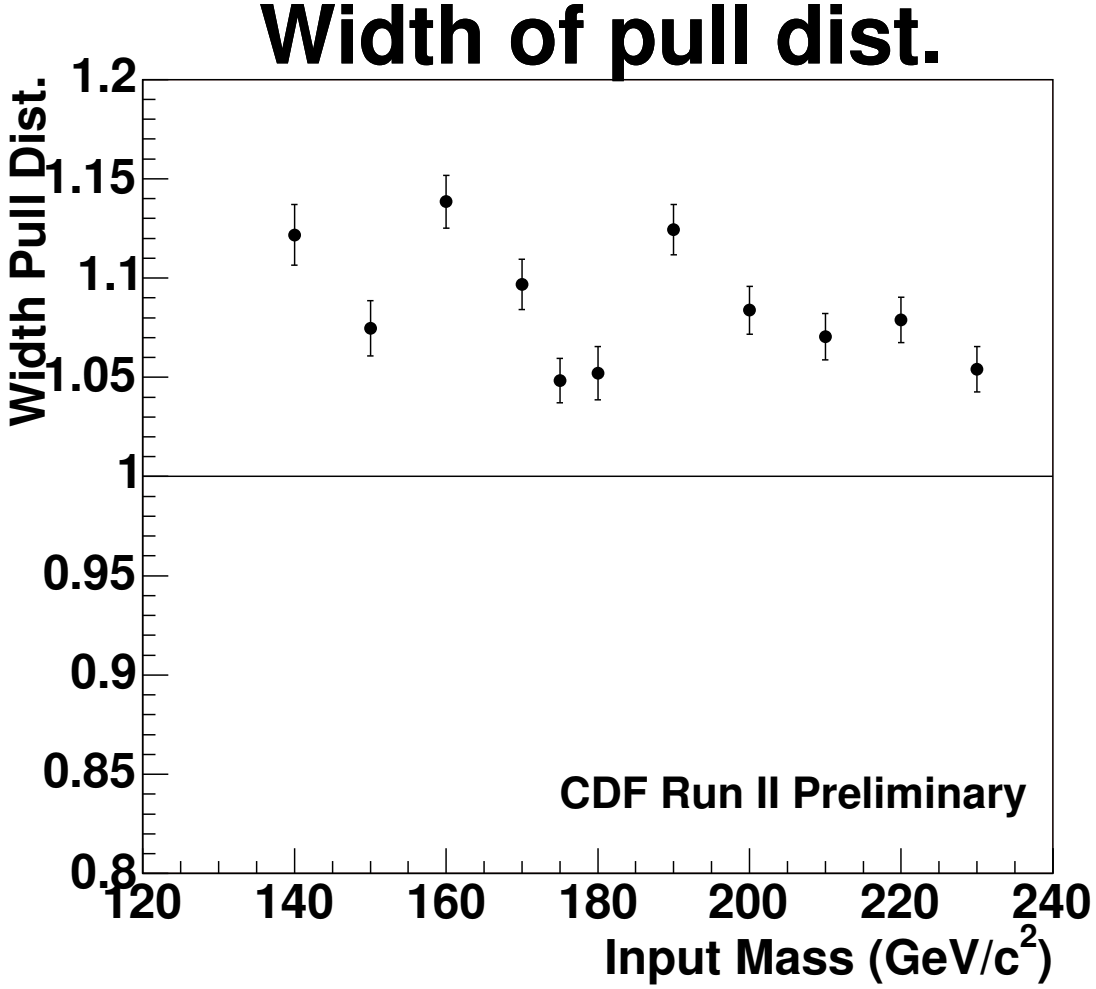

FIG. 16: The Gaussian width of pull distributions from 10,000 pseudoexperiments as a function of true top quark mass. The error bars come mostly from the limited statistics of the Monte Carlo samples from which the pseudodata is taken.

2. Results of Combined Likelihood

Finally, the likelihood is maximized with respect to all parameters using all four subsamples. The result, after scaling the $\Delta(\ln L) = +1/2$ errors as described in section IV C, is 176.7 $^{+6.0}_{-5.4}$ (stat.) GeV/c^2. The combined likelihood as a function of top mass is shown in Fig. 21. For each value of the top mass in the curve, the likelihood is maximized with respect to all other parameters.

The input constraints and fit results for the combined fit are given in Table VII. Figure 22 shows the consistency of the reconstructed mass distribution in each subsample with the

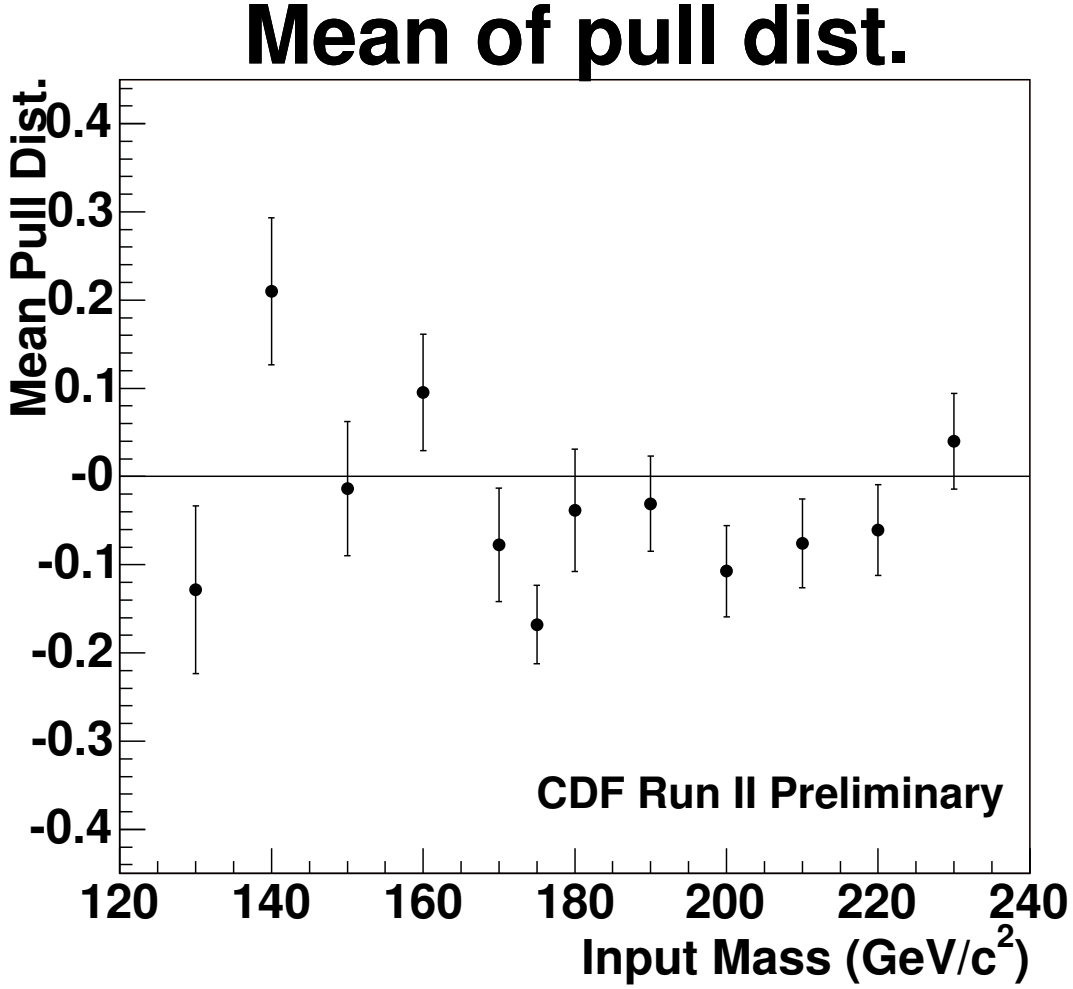

FIG. 17: The Gaussian mean of pull distributions from 10,000 pseudoexperiments as a function of true jet energy scale. The error bars come mostly from the limited statistics of the Monte Carlo sample from which the pseudodata is taken.

combined fit results.

V. SYSTEMATIC UNCERTAINTIES

Systematic uncertainties arise from uncertainties in our understanding of the detector response, and in the assumptions employed to infer a top quark mass from the observed data. The magnitudes of such uncertainties are estimated using auxiliary data collected for this purpose, and large samples of Monte Carlo simulated events that allow us to measure the sensitivity of the measurements to reasonable variations in analysis assumptions.

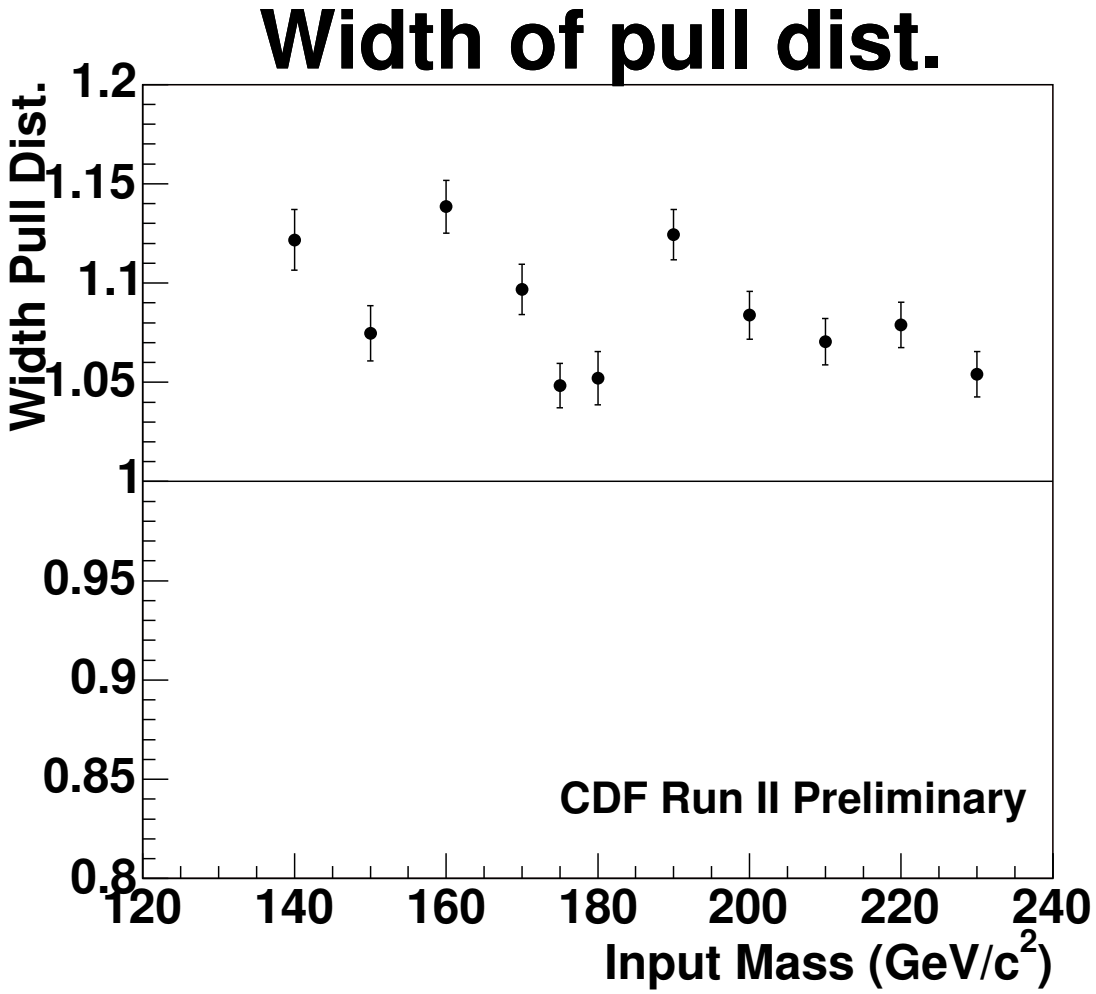

FIG. 18: The Gaussian width of pull distributions from 10,000 pseudoexperiments as a function of true jet energy scale. The error bars come mostly from the limited statistics of the Monte Carlo samples from which the pseudodata is taken.

For each source of systematic uncertainty, the relevant quantities or parameters are varied by $\pm 1\sigma$, and new 175 GeV/c^2 $t\bar{t}$ signal and background Monte Carlo templates are produced by performing event selection and mass reconstruction on the modified samples. Events for pseudoexperiments (see section IV C) are taken from these new templates, but the signal and background p.d.f.'s used in the analysis remain unchanged. The shift in the median fitted top mass for a large ensemble of pseudoexperiments is taken as the systematic uncertainty associated with a given assumption or effect. When the uncertainty on a given systematic shift due to the statistics of the Monte Carlo sample is larger than the shift itself, the

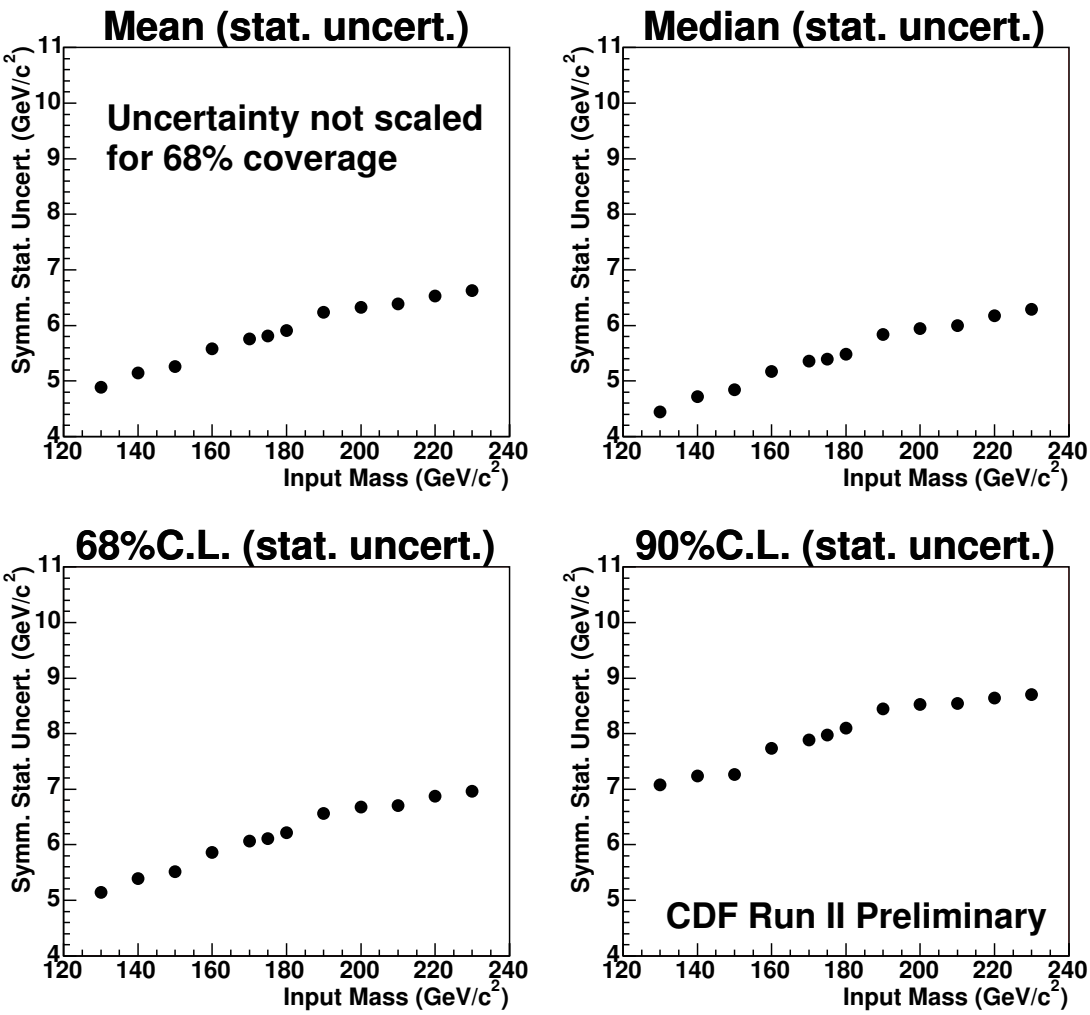

FIG. 19: The mean, median, 68th percentile, and 90th percentile of the symmetrized statistical errors from 10,000 pseudoexperiments are shown as a function of the input top mass.

uncertainty is used as the systematic uncertainty.

A. Jet Systematic Errors

There are significant uncertainties on many aspects of the measurement of jet energies. Some of these are in the form of uncertainties on the energy measurements themselves; some are uncertainties on the detector simulation, which is used to derive many corrections, and ultimately to extract the top mass; still others are best understood as uncertainties on jet production and fragmentation models used in the generators. The jet energy systematic errors, as well as the procedure to evaluate the resulting systematic uncertainty on the top

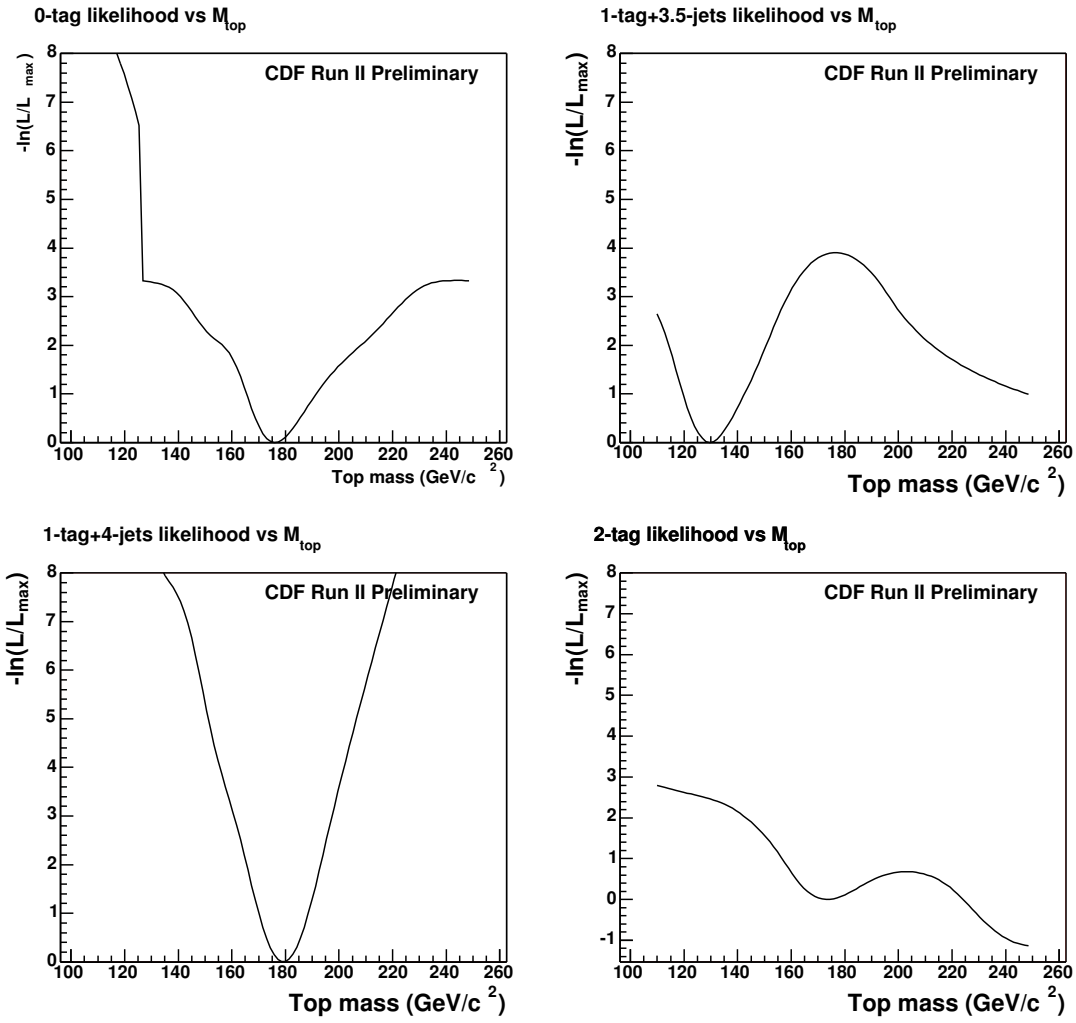

FIG. 20: The negative log-likelihood curves as a function of top mass are shown for the independent fit to each subsample in the data. Upper left: 2-tag events; upper right: 1-tag(T) events; lower left: 1-tag(L) events; lower right: 0-tag events.

mass measurement, are described in this section.

The uncertainties discussed in this subsection are relevant to the top mass measurement made using only the jet energy scale calibration determined independently from the top quark mass sample. They are not relevant to the *in situ* jet energy scale determination, which are described in the following section.

Response relative to central The systematic uncertainties in the calorimeter response relative to the central calorimeter are summarized in Table VIII. The uncertainties for data account for the residual η dependence after dijet balancing, biases in the dijet

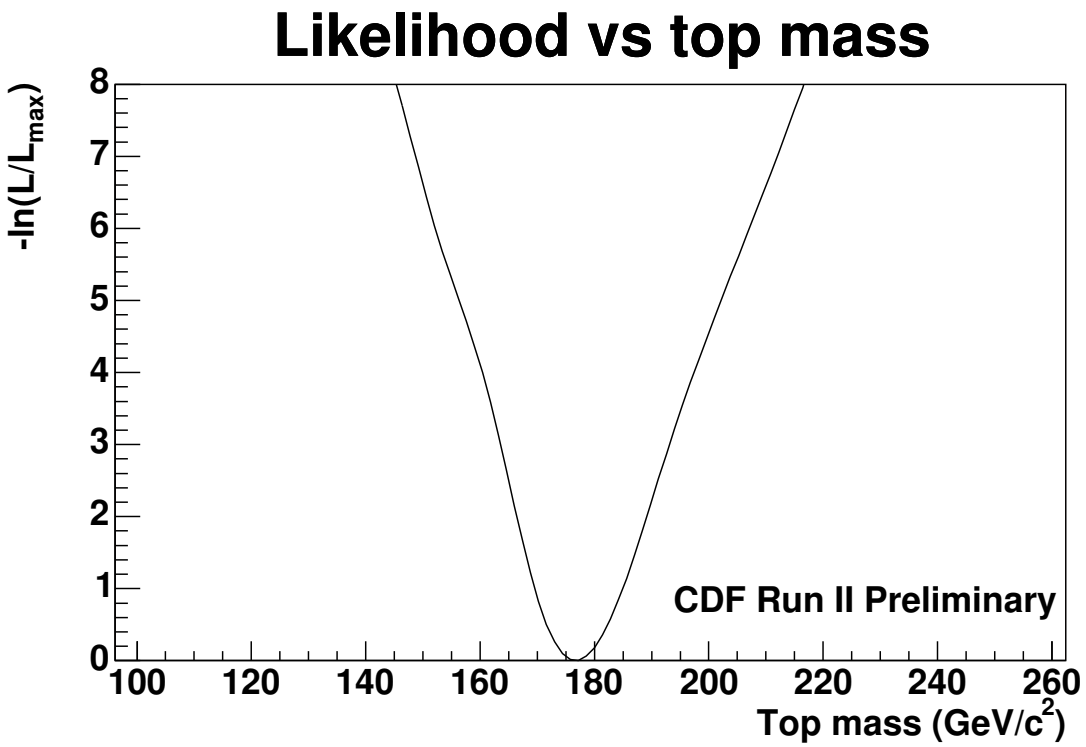

FIG. 21: The negative log-likelihood curve as a function of top mass for the combined fit. For each top mass along the x axis, the likelihood is maximized with respect to all other free parameters.

balancing procedure, especially near the uninstrumented regions, and the variation of the plug calorimeter response with time. Half the difference between the relative response in data jets and simulated jets is taken as a systematic uncertainty for the simulated jets. Photon-jet balancing is used to check the η dependence after corrections in data and simulated events (see Fig. 23).

Central Calorimeter Response A systematic uncertainty is associated with the single-particle response of the central calorimeter. The difference between run I and run II energy scales is studied using photon-jet balancing and is measured to be 5%, at least 2% of which comes from a difference in the CEM scale definition and additional material in the run II tracking volume, which results in a softer particle spectrum due to external brehmsstrahlung and conversions. The remaining 3% difference is taken as a systematic uncertainty on the data jet energies.

A separate comparison of the photon-jet balancing in data and simulation (see Fig. 23) finds a maximal difference of 5% between the two. Subtracting the data uncertainty of

TABLE VII: The input constraints and fitted values (with errors from $\Delta(\ln L) = +1/2$) are given for all free parameters in the combined likelihood fit.

Category		2-tag	1-tag(T)	1-tag(L)	0-tag
M_{top}	constraint	None			
	raw fit	$176.7\ ^{+5.7}_{-5.1}$ (stat.) GeV/c^2			
	scaled fit	$\mathbf{176.7\ ^{+6.0}_{-5.4}}$ (stat.) GeV/$\mathbf{c^2}$			
n_s	constraint	None	None	None	None
	fit	1.8 ± 1.4	15.4 ± 4.3	0.0 ± 3.0	18.2 ± 8.2
n_b	constraint	0.18 ± 0.02	2.7 ± 0.6	3.9 ± 0.7	24.5 ± 7.1
	fit	0.18 ± 0.04	2.7 ± 0.6	3.7 ± 0.7	22.3 ± 6.3

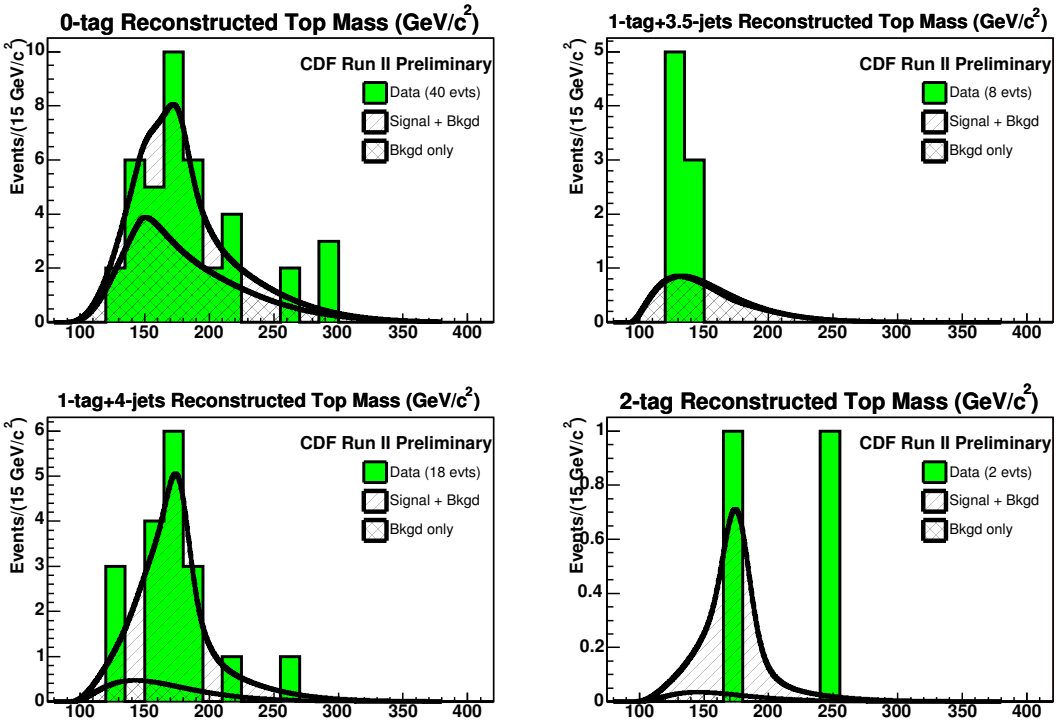

FIG. 22: The reconstructed mass distribution for each subsample is shown overlaid with the expected distribution using the top mass, signal normalization, and background normalization from the combined fit.

TABLE VIII: η-dependent systematic uncertainties on jet energies are shown for data and simulated events.

η range	Jet energy uncertainty	
	Data	Simulation
$\lvert\eta\rvert < 0.2$	3%	1%
$0.2 < \lvert\eta\rvert < 0.6$	0.5%	1%
$0.6 < \lvert\eta\rvert < 1.0$	2%	1%
$1.0 < \lvert\eta\rvert < 1.4$	4%	7%
$1.4 < \lvert\eta\rvert < 2.0$	2%	6%
$\lvert\eta\rvert > 2$	7%	7%

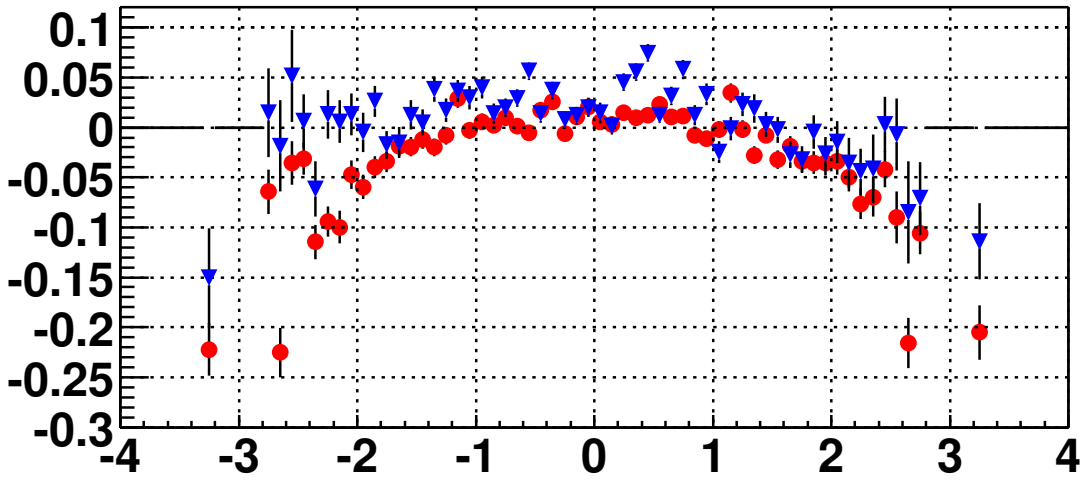

FIG. 23: The balance factor $(p_T^{jet} - p_T^{\gamma})/p_T^{\gamma}$ is shown as a function of η for γ-jet events in data (red circles) and simulation (blue triangles). The jet momenta are corrected for all known effects.

3% in quadrature yields an independent uncertainty of 4% for the simulation energy scale.

Finally, a 1% uncertainty for the stability of the central calorimeter response is assigned.

Correction to Hadrons This systematic error is due to uncertainties in the modeling of jet showering and hadronization, which are tested by varying relevant parameters in the generator. Since the calorimeter response is non-linear, different fragmentation can affect the overall jet energy scale. This uncertainty only accounts for variations

that affect the energy inside the jet cone.

Correction to Partons The uncertainty on the fraction of energy contained in the jet cone (also due to jet fragmentation modeling) is estimated in two parts, one between $R = 0.4$ and $R = 1.0$ and the other between $R = 1.0$ and $R = \infty$.

To determine the systematic uncertainty on the top quark mass measurement given the various sources defined above, the mass shifts for $+1\sigma$ and -1σ perturbations in the jet energies are extracted as described above, and a symmetric uncertainty for each source is defined as half the difference between the two shifts.

Table IX lists the uncertainties obtained for the top mass measurement. The total systematic uncertainty in the top mass due to jet energy measurements is 6.8 GeV/c^2 for the combined measurement. The corresponding systematic uncertainties for an independent measurement in each subsample are listed for comparison.

B. Systematic Uncertainties Arising from the JES Calibration

The use of the observed W boson mass to constrain the jet energy scale calibration essentially measures the average energy response of light quark jets arising from the decay of the colourless W boson. However, the top mass also depends on the energy response to b quark jets. This introduces three possible sources of uncertainty: i) uncertainties in energy response arising from uncertainties in the decay properties of bottom quarks, ii) uncertainties arising from possible variations in the fragmentation properties of bottom quarks, and iii) uncertainties in energy response arising from the different colour flow associated with bottom quark jets produced in top quark decay.

We varied the bottom quark semi-leptonic branching fractions in our Monte Carlo models to understand the effect of this uncertainty in the overall energy scale of the bottom quark jet. We found that this introduced an additional uncertainty in the bottom quark jet energy scale of 0.4% resulting in an uncertainty in the extraction of the top quark mass of 0.4 GeV/c^2. We used the high-statistics measurements of bottom quark fragmentation observed in $Z \to b\bar{b}$ decays at the LEP Collider to constrain the possible fragmentation models in our Monte Carlo calculations. We found that this variation introduced an additional top quark mass uncertainty of 0.4 GeV/c^2. In order to test the effects of possible variations in energy

TABLE IX: The uncertainties on the top mass measurement are shown for each jet energy systematic error. Estimates are obtained for the independent subsamples as well as for the combined measurement. ***We do not have all these numbers for the currently blessed analysis. Only the bottom right number is real, others are guesses for now.***

Jet energy systematic				
		ΔM_{top} (GeV/c^2)		
2-tag	1-tag(T)	1-tag(L)	0-tag	Combined
Response relative to central				
2.5	3.0	2.8	3.5	3.0
Central calorimeter response				
4.0	5.0	4.7	6.0	5.0
Corrections to hadrons (absolute scale)				
2.0	2.2	2.1	2.5	2.2
Corrections to partons (out-of-cone)				
2.0	2.2	2.1	2.5	2.2
Total systematic due to jet energies				
5.8	6.3	6.5	8.3	6.8

response due to different models of "colour flow" in the top quark production and decay, we varied the parameters of the algorithms used to generate this colour flow in both HERWIG and Pythia and conservatively estimated that this could result in an uncertainty in the bottom quark jet energy scale of 0.3%. This results in an additional uncertainty in the top quark mass of 0.3 GeV/c^2.

We add these three contributions in quadrature and include an additional 0.6 GeV/c^2 systematic uncertainty in the top quark mass arising from the modelling of the bottom quark jets.

C. ISR/FSR/PDF Systematic Errors

The systematic uncertainties due to initial state radiation, final state radiation, and parton density functions are summarized in Table X, and detailed below.

Extra jets originating from the incoming partons and outgoing partons affect the measurement of M_{top} when they are misidentified as jets from the final state partons or change the kinematics of the final state partons. ISR and FSR are controlled by the same DGLAP evolution equation that tells us the probability for a parton to branch [**? ? ? ? ?**]. ISR is studied using Drell-Yan events in dilepton channels. The advantage of Drell-Yan events is that there is no FSR, and they are produced by the $q\bar{q}$ annihilation process, as are $t\bar{t}$ pairs (85% by $q\bar{q}$).

The level of ISR is measured as a function of the Drell-Yan mass scale and shows a logarithmic dependence on the Drell-Yan mass squared, as shown in Fig. 24. By extrapolation, the ISR effect is then estimated at top pair production energies. Based on this measurement, two ISR systematic Monte Carlo samples ($+1\sigma_{ISR}$ and $-1\sigma_{ISR}$) are produced using Pythia, by varying the value of Λ_{QCD} and the K factor to the transverse momentum scale for ISR showering. The parameters used are $\Lambda_{QCD} = 384$ MeV, $K = 0.5$ for $+1\sigma_{ISR}$ and $\Lambda_{QCD} = 100$ MeV, $K = 2.0$ for $-1\sigma_{ISR}$. The corresponding curves of Drell-Yan dilepton $\langle p_T \rangle$ vs invariant mass squared are shown in Fig. 24. Although ISR is also sensitive to the choice of parton distribution function (PDF), the PDF uncertainty is not included as a part of the ISR uncertainty. Because a PDF change affects not only ISR but also hard scattering kinematics, the PDF uncertainty is treated separately. Since ISR and FSR shower algorithms are the same, the same variations in Λ_{QCD} and K are used to generate FSR systematic samples. The largest top mass shift between default Pythia and the two ISR samples, 1.2 GeV/c^2, is taken as the ISR uncertainty. Using the same method, 1.2 GeV/c^2 is determined as the FSR uncertainty as well.

The calculation of the top quark invariant mass does not in principle depend on the choice of input PDF, as long as the jets from final state $t\bar{t}$ partons are used. However, changing the PDF changes the top quark η and p_T distributions as well as the size of ISR. The result is a change in the probability of selecting the correct jets, which affects the reconstructed invariant mass of the top quark.

To examine the systematic effect due to PDF uncertainties, 20 pairs of uncertainty sets based on CTEQ6M are used [**? ?**]. These PDFs provide "$\pm 1\sigma$" variations for 20 independent eigenvectors, but do not include variation in Λ_{QCD}. The difference between MRST72 (Λ_{QCD} =228 MeV) and MRST75 (Λ_{QCD} =300 MeV) is included as an addtional uncertainty. Instead of 42 different, fully simulated sets of events, a single simulated sample is used, and

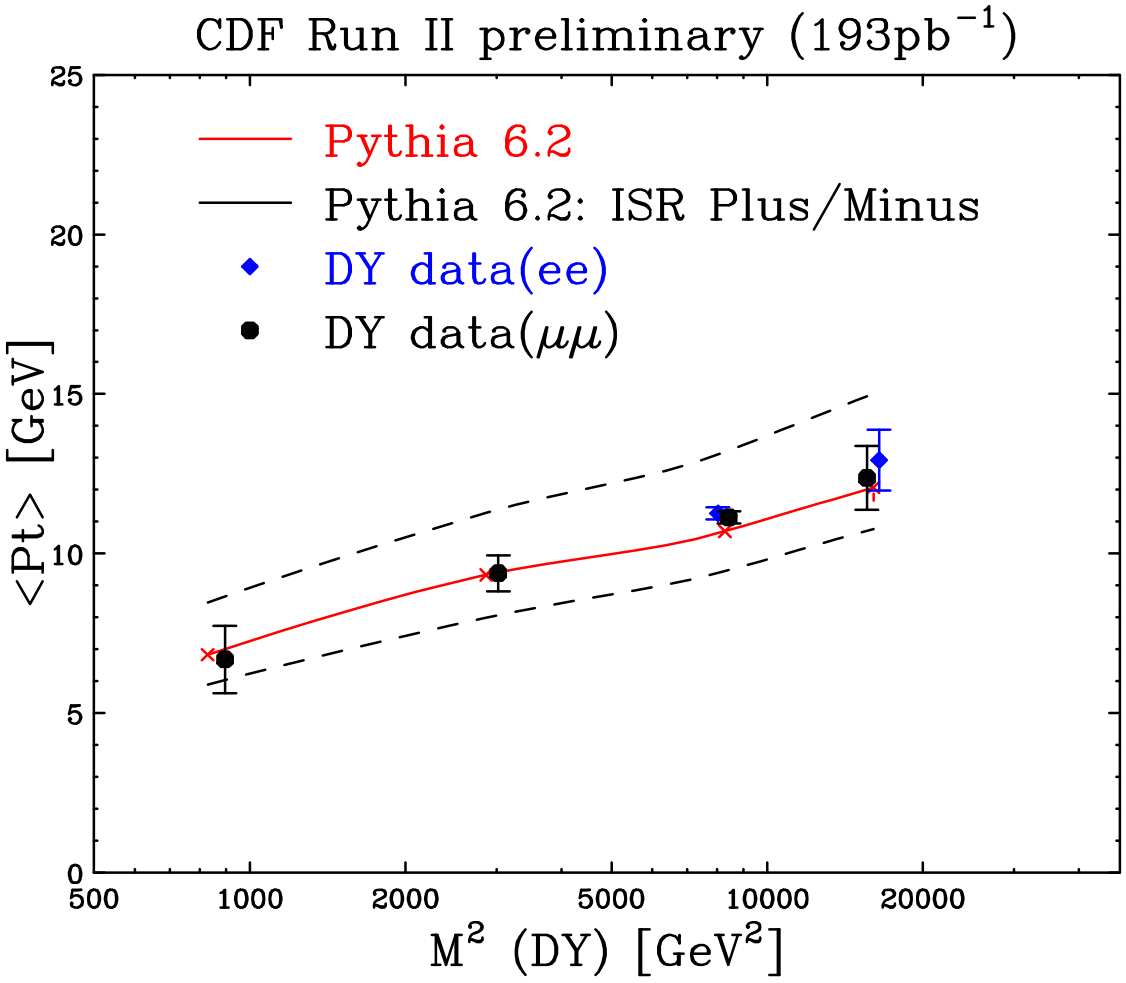

FIG. 24: The average p_T of the dilepton system, which corresponds to the level of ISR activity, shows a logarithmic dependence on the dilepton invariant mass M_{ll}^2. The data are compared with the predictions of Pythia 6.2 and of the $+1\sigma_{ISR}$ and $-1\sigma_{ISR}$ samples.

mass templates are generated for the different PDF sets by weighting events according to the probability of observing their incoming partons using each PDF set. This technique also removes the uncertainty due to limited Monte Carlo statistics. Half of the difference in top mass for each of the 20 pairs of CTEQ6 PDFs (varying one eigenvector at a time) is added in quadrature for the PDF uncerainty, with an additional systematic error of 0.076 GeV/c^2 from the variation of Λ_{QCD}. The total PDF uncertainty is 0.4 GeV/c^2.

TABLE X: The systematic uncertainties on the top mass measurement are shown corresponding to initial and final state radiation, and the choice of parton density functions. Estimates are obtained for the independent subsamples as well as for the combined measurement. ***We do not have all these numbers for the currently blessed analysis. Only the numbers in the right column are real, others are guesses for now.***

Systematic source				
		ΔM_{top} (GeV/c^2)		
2-tag	1-tag(T)	1-tag(L)	0-tag	Combined
Initial state radiation				
1.2	1.2	1.2	1.2	1.2
Final state radiation				
1.2	1.2	1.2	1.2	1.2
Parton density functions				
0.4	0.4	0.4	0.4	0.4

D. Systematic Uncertainties Arising from the W Boson Mass

The use of the observed W boson mass to constrain the jet energy scale calibration assumes that

E. Other Systematic Errors

The remaining systematic sources are described in this section. Table XI gives the summary.

The difference in the top mass between Herwig and Pythia samples is 0.1 ± 0.3 GeV/c^2. To be conservative, this difference is taken as another systematic uncertainty (0.3 GeV/c^2), although the differences in ISR and FSR between the two generators are already taken into account in the ISR and FSR uncertainties, and fragmentation effects are accounted for in the jet energy uncertainties.

The uncertainty in the shape of the background top mass template is dominated by the uncertainty in the Q^2 scale that is used for the calculation of the hard scattering and for

the shower evolution. Different background shapes are obtained for four different Q^2 scales ($4M_W^2$, M_W^2, $M_W^2/4$, and $M_W^2 + P_{TW}^2$) using ALPGEN MC samples. An ALPGEN $Wb\bar{b} + 1$ parton Monte Carlo sample is used for the tagged events and a $W + 3$ parton sample for the 0-tag events. Half of the largest difference in top mass is used as the systematic uncertainty, 1.0 GeV/c^2, which is dominated by the uncertainty in the 0-tag sample.

Although uncertainties in the jet energy scale have been accounted for above, there may also be inconsistencies in the energy resolution for data jets and simulated jets. In fact, photon-jet balancing studies show that simulated jets are roughly 15% narrower than jets in the data. When jets in the simulated $t\bar{t}$ sample are smeared by an extra 15%, the shift in the top mass is 0.5 GeV/c^2, which is taken as a systematic uncertainty due to jet resolution.

Different b-tagging efficiency in data and simulation can introduce a bias in the top quark mass measurement. The E_T^{jet} dependence of the b tagging in data and simulation is consistent with being the same. The effect of $\pm 1\sigma$ in the E_T dependence was found to be only 0.1 GeV/c^2 in run I [**?**]. The same uncertainty is used here.

The analysis can have a systematic bias due to the finite statistics of Monte Carlo samples that are used to obtain the signal and background shape parameterizations. For a rough estimate of this uncertainty, sets of pseudoexperiments are performed with a series of fluctuated signal and background templates; in each fluctuated template, each bin is varied randomly according to Poisson statistics. For each fluctuated template, the median top mass measured by pseudoexperiments is shifted. The typical shift due to these statistical fluctuations, taken as a systematic uncertainty due to Monte Carlo statistics, is 0.3 GeV/c^2.

F. Total Systematic Uncertainty

The systematic uncertainties for the combined measurement are summarized in Table XII. The total systematic uncertainty is estimated to be 7.1 GeV/c^2.

VI. CONCLUSION

We have made a new measurement of the top quark mass,

$$173.5\ ^{+3.7}_{-3.6}\ \text{(stat.)} \pm 1.7\ \text{(syst.)}\ \text{GeV}/c^2,$$

TABLE XI: The remaining systematic uncertainties on the top mass measurement are shown. Estimates are obtained for the independent subsamples as well as for the combined measurement. ***We do not have all these numbers for the currently blessed analysis. Only the numbers in the right column are real, others are guesses for now.***

Systematic source				
		ΔM_{top} (GeV/c^2)		
2-tag	1-tag(T)	1-tag(L)	0-tag	Combined
Background template shape				
0.1	0.3	0.2	1.2	1.0
Tagging efficiency				
0.2	0.1	0.1	—	0.1
Generators				
1.2	1.2	1.2	1.2	1.2

using a novel technique that utilizes the jet energy scale information provided by the hadronically decaying W boson in the top quark events. This provides one of the most precise single constraints on this important physical parameter. We have performed a cross-check of this result using a more traditional "template" technique that does not use the *in situ* jet energy scale constraint, and found excellent agreement.

This measurement is part of a rich top physics program at CDF. As the luminosity acquired increases from the current 318 pb^{-1} to an expected 4000–7000 pb^{-1} for run II, the statistical uncertainty will improve. The systematic uncertainty will also be reduced till we approach statistical uncertainties of approximately 2.0 GeV/c^2, at which point the uncertainties on initial and final state radition, as well as bottom quark jet energy scale become comparable to the statistical uncertainties associated with the top quark mass and jet energy scale measurement. More top quark mass results from CDF are being published concurrently [**?**]. We expect that these will provide important inputs into our understanding of the fundamental fermions and the nature of the electroweak interaction.

TABLE XII: This table summarizes all systematic uncertainties for the combined analysis.

Source of Systematics	ΔM_{top} (GeV/c^2)
Jet Energy	6.8
ISR	1.2
FSR	1.2
PDFs	0.4
Generators	0.3
Background Shape	1.0
Jet Resolution	0.5
b tagging	0.1
MC statistics	0.3
Total	7.1

Acknowledgments

We thank the Fermilab staff and the technical staffs of the participating institutions for their vital contributions. This work was supported by the U.S. Department of Energy and National Science Foundation; the Italian Istituto Nazionale di Fisica Nucleare; the Ministry of Education, Culture, Sports, Science and Technology of Japan; the Natural Sciences and Engineering Research Council of Canada; the National Science Council of the Republic of China; the Swiss National Science Foundation; the A.P. Sloan Foundation; the Bundesministerium fuer Bildung und Forschung, Germany; the Korean Science and Engineering Foundation and the Korean Research Foundation; the Particle Physics and Astronomy Research Council and the Royal Society, UK; the Russian Foundation for Basic Research; the Comision Interministerial de Ciencia y Tecnologia, Spain; and in part by the European Community's Human Potential Programme under contract HPRN-CT-20002, Probe for New Physics.